Atlas-Guided Discovery of Transcription Factors for T Cell Programming

H. Kay Chung[1,2,3*#], Cong Liu[4*], Anamika Battu[2], Alexander N. Jambor[4], Brandon M. Pratt[2,9], Fucong Xie[2], Brian P. Riesenberg[2], Eduardo Casillas[1], Ming Sun[1], Elisa Landoni[2], Yanpei Li[2], Qidang Ye[2], Daniel Joo[2], Jarred Green[2], Zaid Syed[2], Nolan J. Brown[2], Mattew Smith[2], Shixin Ma[1], Shirong Tan[1], Brent Chick[5], Victoria Tripple[1], Z. Audrey Wang[2,4], Jun Wang[4], Bryan Mcdonald[1], Peixiang He[6,7], Qiyuan Yang[1], Timothy Chen[1], Siva Karthik Varanasi[1], Michael LaPorte[1], Thomas H. Mann[1], Dan Chen[1], Filipe Hoffmann[1], Josephine Ho[5], Jennifer Modliszewski[2], April Williams[8], Yusha Liu[2], Zhen Wang[11], Jieyuan Liu[11], Yiming Gao[12], Zhiting Hu[11], Ukrae H. Cho[2,3], Longwei Liu[6,7], Yingxiao Wang[6], Diana C. Hargreaves[5], Gianpietro Dotti[2,10], Barbara Savoldo[2,10], Jessica E. Thaxton[2,3], J. Justin Milner[2,10], Susan M. Kaech[1#], Wei Wang[4#]

[1]NOMIS Center for Immunobiology and Microbial Pathogenesis, Salk Institute for Biological Studies, La Jolla, CA, USA
[2]Lineberger Comprehensive Cancer Center, University of North Carolina at Chapel Hill, Chapel Hill, NC, USA
[3]Department of Cell Biology & Physiology, University of North Carolina at Chapel Hill, Chapel Hill, NC, USA
[4] Department of Chemistry and Biochemistry, University of California San Diego, La Jolla, CA, USA.
[5] Molecular and Cell Biology laboratory, Salk Institute for Biological Studies, La Jolla, CA, USA
[6]Alfred E. Mann Department of Biomedical Engineering, University of Southern California, Los Angeles, CA, USA
[7]Department of Bioengineering, Institute of Engineering in Medicine, University of California, La Jolla, CA, USA
[8]Razavi Newman Integrative Genomics and Bioinformatics Core, Salk Institute for Biological Studies, La Jolla, CA, USA
[9]Department of Pharmacology, University of North Carolina at Chapel Hill, Chapel Hill, NC, USA.
[10]Department of Microbiology and Immunology, University of North Carolina at Chapel Hill, Chapel Hill, NC, USA.
[11]Halıcıoğlu Data Science Institute, University of California San Diego, La Jolla, CA, USA.
[12]Department of Electrical & Computer Engineering, Texas A&M University
* Equal contribution, # Co-corresponding

$CD8^+$ T cells differentiate into diverse states that shape immune outcomes in cancer and chronic infection[1–4]. To systematically define the transcription factors (TFs) driving these states, we built a comprehensive atlas integrating transcriptional and epigenetic data across nine $CD8^+$ T cell states and inferred TF activity profiles. Our analysis catalogued TF activity fingerprints, uncovering regulatory mechanisms governing selective cell state differentiation. Leveraging this platform, we focused on two transcriptionally similar but functionally opposing states critical in tumor and viral contexts: terminally exhausted T cells (TEX_{term}), which are dysfunctional[5–8], and tissue-resident memory T cells (T_{RM}), which are protective[9–13]. Global TF community analysis revealed distinct biological pathways and TF-driven networks underlying protective versus dysfunctional states. Through *in vivo* CRISPR screening integrated with single-cell RNA sequencing (*in vivo* Perturb-seq), we delineated several TFs that selectively govern TEX_{term} differentiation. We also identified HIC1 and GFI1 as shared regulators of TEX_{term} and T_{RM} differentiation and KLF6 as a unique regulator of T_{RM}. Importantly, we discovered novel TEX_{term}-selective TFs, including ZSCAN20 and JDP2, with no prior known function in T cells. Targeted deletion of these TFs enhanced tumor control and synergized with immune checkpoint blockade but did not interfere with T_{RM} formation. Consistently, their depletion in human T cells reduces the expression of inhibitory receptors and improves effector function. By decoupling exhaustion T_{EX}-selective from protective T_{RM} programs, our platform enables more precise engineering of T cell states, accelerating the rational design of more effective cellular immunotherapies.

Cell states are the range of cellular phenotypes arising from a defined cell type's interaction with its environment. Within the immune system, T cells possess multiple differentiation states, particularly as naive T cells differentiate into diverse states with different functionality and trafficking patterns in various immune environments, such as tumors and virus infections[1–4]. As transcription factors (TFs) govern cell state differentiation[14], understanding how TFs shape these states is essential for programming beneficial states with therapeutic potential. One promising application of cell state engineering is enhancing $CD8^+$ T cells for adoptive cell transfer therapy (ACT) of tumor-infiltrating lymphocytes (TILs) or CAR-T cells. However, identifying TFs that control $CD8^+$ T cell states is difficult due to substantial heterogeneity and overlapping transcriptomes, even between functionally divergent states.

We focused on two transcriptionally similar yet functionally divergent states: the protective tissue-resident memory (T_{RM}) cell state and the dysfunctional terminally exhausted (TEX_{term}) cell state. Many studies show that TILs with T_{RM} characteristics correlate with better survival in solid tumor patients[9–13]. Conversely, during persistent antigen stimulation scenarios such as chronic virus infection (e.g., HIV) or cancer, T cells progressively express diverse inhibitory receptors, including PD1, lose memory potential, and effector functions. This process is known as T cell exhaustion (TEX)[5,7,8,15], and cells in this trajectory eventually adopt the TEX_{term} cell state. TEX_{term} cells express higher levels of diverse inhibitory receptors (e.g., TIM3 and CD101), lack effector and proliferative capacity, and do not respond effectively to immune checkpoint blockade (ICB), such as anti-PD1 monoclonal antibody (mAb) blockade[16–18]. High TEX_{term} marker expression often indicates poor prognosis in solid tumors, though some markers also correlate with ICB response, highlighting their complex role in tumor immunity[19,20]. Despite their distinct functional impact on cancer outcomes, TEX_{term} and T_{RM} cells both preferentially reside in tissues[1,3] and display remarkable similarities in their transcriptional profiles, including key regulatory TFs such as BLIMP1[5,21–23], BHLHE40[24,25], and NR4A2[9,26,27](Fig. 1a,b, Extended Data Fig. 1a-c). These two cell states even exhibit highly correlated open chromatin regions (Extended Data Fig. 1d), complicating the precise identification of TFs whose disruption may selectively inhibit TEX_{term} while preserving T_{RM} cell development. Given that many TFs are commonly expressed across different $CD8^+$ T cell states and differentiation trajectories, a sophisticated and precise bioinformatics approach is crucial to pinpoint the bona fide cell-state-specifying TFs essential for T cell programming.

We hypothesized that identifying key TFs controlling selective CD8$^+$ T cell differentiation can be achieved through systematic comparison of TF activity across the differentiation landscape. Accurate prediction requires recognizing that TF activity does not necessarily mirror expression, as it depends on post-translational modifications, cofactors, and target accessibility[28], and that TF effects propagate through genetic networks. We therefore developed a multi-omics atlas integrating transcriptomic and chromatin data from nine CD8$^+$ T cell states to understand "global" influences of TFs in each cell state and to identify "*selective*" or "*shared*" TFs. Our atlas-based platform can map TF communities and their target genes ("regulatees"), guiding state-specific differentiation.

Multiomics atlas maps of CD8$^+$ T Cell TFs

Our initial objective was to create a comprehensive catalogue of TF activity across diverse CD8$^+$ T cell states by integrating our TF activity analysis pipeline, Taiji[29–31], with comparative statistical analysis. In Taiji, the gene regulatory network (GRN) is a weighted, directed network that models regulatory interactions between TFs and their target genes. In this GRN, each node corresponds to a gene, and its weight is proportional to the gene's expression level. Each edge represents a regulatory interaction and is weighted based on a combination of factors: the TF's predicted binding affinity to the target gene, the chromatin accessibility at the target gene's locus, and the expression levels of both the TF and the target gene (Fig. 1c)[29,30]. To determine the global influence of each TF within the network, Taiji applies a personalized PageRank algorithm, which assigns an "importance" score to each node based on both the quantity and quality of incoming connections. This approach yields a measure of TF activity that reflects the influence of each TF in the broader regulatory landscape, accounting for upstream regulators, downstream targets, and feedback loops through iterative computation.

With Taiji, we previously identified TFs involved in pan-immune lineage commitment, including NK cells, dendritic cells, B cells, and γδ T cells[35]. While earlier studies provided foundational insights into cell differentiation, a more refined analysis within CD8$^+$ T cells is needed to achieve higher resolution of TF roles. Therefore, leveraging the improved statistical filtering, we aimed to quantify the global influence of TFs across all CD8$^+$ T cell states.

To begin, we analyzed ATAC-seq and RNA-seq datasets from 121 CD8$^+$ T cell samples spanning nine distinct states, using both previously published and newly generated datasets from well-characterized

acute and chronic lymphocytic choriomeningitis virus (LCMV) infections[3,9,18,23,32–36] (Extended Data Fig. 2; Supplementary Table 1). In acute LCMV-Armstrong infections, $CD8^+$ T cells differentiate into memory precursor (MP), terminal effector (TE), effector memory (T_{EM}), central memory (T_{CM}), and T_{RM} states. In chronic LCMV-Clone 13 infections, they adopt heterogeneous exhaustion cell states, including progenitors of exhaustion (TEX_{prog}), effector-like exhaustion (TEX_{eff}), and TEX_{term}.

Next, we conducted an unbiased comparative analysis using statistical filtering to understand the specificity of TF activity across the $CD8^+$ T cell states (Extended Data Fig. 2a, Supplementary Table 2). This identified TFs; 136 were predominantly '**single-state**' TFs, with each cell state selectively containing 12-19 unique TFs (Fig. 1d, Extended Data Fig. 2b). This category included novel TFs such as *Hoxa7* in Naïve, *Snai1* in T_{RM}, *Hey1* in TEX_{prog}, *Sox8* in TEX_{eff}, and *Zscan20* and *Jdp2* in TEX_{term} cells. In contrast, 119 TFs were key regulators in more than one cell state, termed '**multi-state'** TFs (Fig. 1e), such as *Tcf7* and *Tbx21*. *Tcf7* is a known driver of Naive-, MP-, and TEX_{prog} states, all multipotent with high proliferative capacity[3,18]. Multi-state TFs like *Vax2*, *Batf*, *Irf8*, and *Stat1* were more enriched within the exhaustion-associated cell states (TEX_{prog}, TEX_{eff}, and TEX_{term}). Consistent with TEX_{term} and T_{RM} similarity (Fig. 1b; Extended Data Fig. 1b-d), both cell states share the most TFs compared to other cell states (e.g., *Egr2*, *Crem*, *Prdm1*, Extended Data Fig. 2c).

While Taiji provides a statistically grounded approach for inferring TF activity, there is no absolute threshold for defining cell state specificity, and some misclassification is expected, particularly for TFs with overlapping functions or modest differences in activity. Still, Taiji is useful to highlight TFs with activity patterns enriched in specific cell states. For instance, although *Eomes* was classified as a TEX_{term} single-state TF herein, it also functions in effector, T_{EM}, T_{CM}, and T_{RM} differentiation[37,38]. This illustrates that more accurate classifications require further investigation and resolution, as performed herein for several TFs.

TF state-selectivity in TEX_{term} and T_{RM} cells

Despite the strong transcriptional overlap between TEX_{term} and T_{RM} cells, our Taiji pipeline predicted TFs selectively active in either of these two cell states. This could aid in developing better immunotherapies, in which one can engineer T cells away from exhaustion and toward more functional effector cell states without negatively impacting T_{RM} formation in tissues and tumors. Based on

statistical criteria (Extended Data Fig. 2a), we identified 20 and 34 TFs as single-state TFs of T_{RM} or TEX_{term} cells, respectively, and 30 multi-state TFs active in both (Fig. 1f–h; Extended Data Fig. 2a, blue boxes; Supplementary Table 3). TEX_{term} single-state TFs included many previously unreported TFs such as *Zscan20*, *Jdp2*, *Zfp324*, *Zfp143*, *Zbtb49*, and *Arid3a* (Fig. 1f). T_{RM} single-state TFs included *Fosb*, *Zfp692*, *Atf4*, *Pbx4*, *Junb*, *and Klf6* (Fig. 1g). Of the TEX_{term} and T_{RM} multi-state TFs, some were well-known to function in the development of *both* cell states, such as *Nr4a2*[12], *Bhlhe40*[24], *Prdm1*[23,35], whereas others such as *Hic1*[39] and *Gfi1*[40] were not, identifying them as new multi-state TFs to consider (Fig. 1h). We analyzed previously reported TFs such as cJUN, BATF/BATF3, and TFAP4 that were identified from functional screening of $CD8^+$ T cells[41–44] based on limited phenotypic readouts. These prior screens tended to identify broadly active, multi-state TFs (see Fig. 1). In contrast, our platform enabled a computationally guided, multi-state screen that revealed TFs predicted to have greater state-selective activity (Extended Data Fig. 2d).

To evaluate the predicted TFs governing selective T cell differentiation, we identified dynamic activity patterns of TF groups, termed "TF waves" (Extended Data Fig. 3). TF waves reveal possible combinations of TFs that coordinate trajectories. Seven TF waves linked to specific biological pathways were identified, such as the T_{RM} TF wave (Fig. 1i), including several members of the AP-1 family (e.g., *Atf3*, *Fosb*, and *Jun*) is uniquely associated with the TGFβ response pathway (Extended Data Fig. 4e). The TEX TF wave, involving *Irf8*, *Jdp2*, *Nfatc1*, and *Vax2*, correlates with PD1 and senescence pathways (Fig. 1j, Extended Data Fig. 3e).

TF community analysis of T_{RM} vs TEX_{term} cells

To uncover transcriptional programs governing T_{RM} or TEX_{term} differentiation, we constructed TF–TF association networks capturing functional relationships between TFs (Fig. 2a). Analysis of regulatee-based adjacency matrices (i.e., predicted TF-target gene circuits) revealed shared and distinct patterns of TF collaboration across the two states. Single-state TFs displayed strong intra-state connectivity. TEX_{term} TFs (ZSCAN20, JDP2, ZFP324, IRF8) formed dense networks within TEX_{term} cells (Fig. 2b; Extended Data Fig. 4a), while T_{RM} TFs (FOSB, SNAI1, KLF6) interacted mainly within T_{RM} networks Extended Data Fig. 4b). Interestingly, multi-state TFs (HIC1, PRDM1, FLI1, GFI1), active in both states and previously reported TFs (cJUN, BATF, and TFAP4) formed distinct partnerships in each cell state, reflecting context-specific regulatory architectures (Fig. 2c; Extended Data Fig. 4c).

We next grouped the TF–TF association networks into distinct "TF neighbor communities" in T_{RM} and TEX_{term} cells (Supplementary Table 5), and each community was linked to specific biological processes (Fig. 2d–f). While multi-state TFs shaped overall community topology, single-state TFs drove unique interaction patterns specific to T_{RM} or TEX_{term} cells within each community. Pathway analysis revealed divergent programs in each state—for instance, T_{RM} community-3 was associated with cell adhesion and TGFβ response (Fig. 2e, g, h), while TEX_{term} community-3 was linked to apoptosis (Fig. 2f-h). Community-1 in T_{RM} cells controlled RNA metabolism (Fig. 2e, g, h), whereas in TEX_{term} cells, it was tied to catabolism, proteolysis, and autophagy (Fig. 2f-h).

To assess the functional relevance of state-enriched pathways, we focused on the proteasome pathway, which emerged as a prominent but previously unrecognized feature of TEX_{term} cells (Fig. 2g, h). Proteasome gene signatures were enriched in TEX_{term}-like $CD8^+$ T cells from NSCLC patients[45] and murine MCA-205 TILs (Extended Data Fig. 5a,b). Consistently, proteasome activity—measured by a validated fluorescent probe[46]—was highest in TEX_{term} cells from chronic LCMV (Fig. 2i) and in tumor-specific TILs (Fig. 2j, k) relative to bystander OT-1 cells (Fig. 2k). To test if high proteasome activity correlates with dysfunction, we sorted OT-1 cells by proteasome activity probe intensity and adoptively transferred them into B16F10-OVA tumor-bearing mice. $Proteasome^{high}$ cells showed reduced tumor control compared to $proteasome^{low}$ cells (Fig. 2l), a trend also seen in endogenous TILs (Extended Data Fig. 5c). These findings support the TF-TF network and pathway predictions and identify the proteasome pathway as a functional hallmark of TEX_{term} cells.

In vivo CRISPR Screens of TEX_{term} TFs

The Taiji pipeline enabled comparative analysis of TF activity and curated sets of single-state TFs specific to T_{RM} *vs.* TEX_{term} cells (Fig. 1f-h). To assess its accuracy, Perturb-seq, combining *in vivo* CRISPR screening with single-cell RNA sequencing (scRNA-seq), was performed in two different animal models for T_{RM} or TEX_{term} differentiation (Fig. 3a and 4a). Our Perturb-seq guide RNA (gRNA) library targeted 19 TFs, including seven TEX_{term} and T_{RM} multi-state TFs and 12 TEX_{term} single-state TFs. The TEX_{term}-TFs included one known TF, *Nfatc1*, and 11 others with high specificity scores but not previously linked to TEX_{term} differentiation (gray boxes Fig. 1f,h). The multi-state TFs included two positive controls (*Nr4a2*, *Prdm1*) and unvalidated multi-state TFs (*Nfil3*, *Hic1*, *Gfi1*, *Ikzf3*, *Stat3*. To

ensure comprehensive screening, four gRNAs per target were expressed in two dual-gRNA retroviral vectors (Extended Data Fig. 6a), along with two control vectors with scramble gRNAs (gScramble). This created a library of 40 dual-gRNA vectors, with 76 TF-gRNAs and 4 gScramble controls (Supplementary Table 6).

Cas9$^+$ P14 CD8$^+$ T cells were transduced with this library and transferred into mice infected with **LCMV-Clone 13**, a model of **chronic infection** and CD8$^+$ T cell exhaustion (*note, recipient mice also expressed Cas9 to prevent rejection of donor cells*). Droplet-based sequencing was performed 18+ days post-transfer to assess sgRNA and transcriptomes of each spleen-derived donor Cas9$^+$ P14 CD8$^+$ T (Fig. 3a), analyzing 17,257 cells with unique gRNA expression.

To determine which TFs impaired TEX$_{term}$ cell differentiation, we first employed uniform manifold approximation and projection (UMAP). Four primary clusters were identified: TEX$_{prog}$, TEX$_{eff}$, and TEX$_{term}$ cells and those in cell cycle (Fig. 3b; Extended Data Fig. 6b,c). All clusters expressed *Tox* and *Pdcd1*, key exhaustion markers, and TEX$_{prog}$ cells were identified by *Tcf7*, *Slamf6*, and *Sell* expression. TEX$_{eff}$ cells expressed effector markers, including *Cx3cr1*, *Klrd1*, *Klrk1*, *Klf2*, and *Zeb2*[2], while TEX$_{term}$ cells expressed high inhibitory receptors and well-established exhaustion markers like *Cd101*, *Cd7*, *Cd38*, *Cd39*, *Cxcr6*, and *Nr4a2*. The cell cycle cluster was noted for its expression of *Birc5*, *Mki67*, *Stmn1*, and *Tuba1b*.

Next, we evaluated the impact of individual TF depletion by analyzing the distribution of gRNA$^+$ cells across exhaustion states (Fig. 3c,d). CRISPR KO of the majority of the 19 TEX$_{term}$ driving TFs led to a reduction in TEX$_{term}$ cell frequency. Notably, KOs of multi-state TFs such as *Hic1*, *Stat3*, *Prdm1*, and *Ikzf3* (which encodes AIOLOS) significantly reduced TEX$_{term}$ differentiation by 92% to 89%. Depletion of novel TEX$_{term}$ single-state TFs—including *Zfp324*, *Zscan20*, and *Jdp2*—significantly prevented TEX$_{term}$ differentiation by 78%, 54%, and 43%, respectively (Fig. 3d, bold). Other novel candidates such as *Etv5*, *Arid3a*, *Zfp410*, *Foxd2*, and *Prdm4* also reduced TEX$_{term}$ representation by 25–40%, though some did not reach statistical significance. This Perturb-seq analysis highlights the platform's ability to identify TFs that regulate the TEX$_{term}$ state, with most tested TFs influencing exhaustion to varying degrees.

To further assess how TEX_{term}-driving TF KOs affect $CD8^+$ T cell exhaustion, we used flow cytometry and scRNA-seq to analyze TF KO cells during LCMV-Clone 13 infection (Fig. 3e-i; Extended Data Fig. 6). We tested six TF KOs, including known control (*Prdm1*) and five newly identified TFs (*Zscan20*, *Jdp2*, *Zfp324*, *Stat3*, *Hic1*) that impaired TEX_{term} state differentiation in Perturb-seq. Disrupting these TFs reduced TEX_{term} cell ($PD1^+$ $CX3CR1^-$ $SLAMF6^-$) frequency by ~50% (Fig. 3e, f) and decreased expression of inhibitory receptors such as CD101, CD39, and CD38 (Extended Data Fig. 6d,e). All 19 TEX_{term}-TF KOs exhibited a marked decrease in TEX_{term}-signature genes[47], including *Cd7*, *Cxcr6*, *Nr4a2*, and *Entpd1*(Fig. 3g).

Lastly, the TEX_{term}-driving TF KOs were grouped based on their effects on TEX_{prog} ($PD1^+$ $CX3CR1^-$ $SLAMF6^+$, Fig. 3h) or TEX_{eff} ($PD1^+$ $CX3CR1^+$, Fig. 3i) state differentiation. Loss of *Prdm1* and *Stat3* markedly increased the frequency of TEX_{prog} cells and upregulated TEX_{prog} signature genes (Fig. 3g, h) whereas loss of *Hic1*, *Zscan20*, *Zfp324*, or *Jdp2* primarily expanded the TEX_{eff} cell population and effector signature genes (Fig. 3g, i, j). Deletion of the *Zscan20* and *Jdp2* significantly enhanced effector cytokine production (e.g., IFNγ and TNFα) and reduced viral loads in recipient mice (Fig. 3k, l).

Deleting TEX_{term} TFs Preserves T_{RM} Fate

A major goal of this work was to identify TFs that selectively repress TEX_{term} cell differentiation without affecting T_{RM} differentiation, thereby enabling more precise programming of $CD8^+$ T cell states. Since nearly all the predicted TEX_{term} single-state TFs impaired TEX_{term} differentiation to some degree (Fig. 3), the next step was to evaluate their effects on T_{RM} differentiation to confirm their selective activity. We used the same Perturb-seq library as before, but this time included only the eight TEX_{term} single-state TFs and seven multi-state TFs that impaired TEX_{term} state development by more than 25% in chronic LCMV infection (Fig. 3d). To assess their impact on memory $CD8^+$ T cell development, we isolated RV-transduced $Cas9^+$ P14 $CD8^+$ T cells from the spleen and small intestine (SI) of mice 18 days after **acute LCMV-Armstrong** infection. We then analyzed 15,211 cells using scRNA-seq to determine how these perturbations impacted the formation of intestinal T_{RM} cells, as well as circulating splenic T_{CM} and T_{EM} cells (Fig. 4a).

The UMAP analysis identified four primary clusters containing cells with features of T_{CM} (*Il7r*, *Tcf7*, *Sell*, and *S1pr1)*, T_{EM} (*Cx3cr1*, *Klrg1*, and *Klf2)*, and T_{RM} cells (*Cd69, Cd160, and Itgae* (encoding

CD103)) as well as a small T_{RM} cell population with lower *Itgae*, but higher *Ifng* and *Irf1* expression designated T_{RM} *Itgae*^{low} (Fig. 4b,c; Extended Data Fig. 7a,b)[23,48]. Examination of the gRNA$^+$ cells revealed that none of the eight TEX_{term} single-state TF KOs (*Zfp324*, *Irf8*, *Zfp410*, *Nfatc1*, *Zscan20*, *Jdp2*, *Arid3a*, and *Etv5)* negatively affected T_{RM} formation significantly (Fig. 4d,e, **bold** gene symbols). In fact, KO of *Etv5* tended to increase the frequency of T_{RM} cells. To evaluate the specificity of the TEX_{term} single-state TFs, we also examined the expression of the T_{RM} gene signatures[9,35] in the entire population of gRNA$^+$ cells for each TF tested (Fig. 4f). With the exception of *Etv5* and *Arid3a*, which increased T_{RM}-signature gene expression (Fig. 4f, Extended Data Fig. 7c), perturbation of the TEX_{term} single-state TFs did not substantially alter T_{RM}-signature gene expression. The platform also predicted novel multi-state TFs, including *Hic1* and *Gfi1*. Interestingly, disruption of these multi-state TFs significantly reduced T_{RM} cell frequency (Fig. 4e) and T_{RM}-signature gene expression (Fig. 4f, Extended Data Fig. 7c), mirroring the effects of *Prdm1*, a known multi-state TF for T_{RM} and TEX_{term} cells.

To further validate the Perturb-seq data, we individually depleted the TEX_{term} single-state TFs *Zscan20* and *Jdp2* and multi-state TF *Prdm1* in Cas9$^+$ P14 CD8$^+$ T cells, adoptively transferred them into LCMV-Armstrong infected animals, and assessed their differentiation into T_{CM}, T_{EM}, and T_{RM} cells using flow cytometry (Fig. 4g,h). Deletion of *Zscan20* and *Jdp2* did not alter the formation of any memory cell subtypes, while perturbation of *Prdm1* significantly reduced T_{RM} and increased T_{CM} formation, as expected. Altogether, this multi-omics pipeline predicted TEX_{term} single-state TFs that drive TEX_{term} differentiation without affecting with T_{RM} cell formation and multi-state TFs that influence both cell states. These results demonstrate the accuracy and predictive power of our approach for pinpointing single-state and multi-state TFs.

Klf6 OE drives T_{RM} expansion without inducing exhaustion

To further demonstrate the utility of our cell-state selective TF identification pipeline in discovering novel T_{RM}-associated TFs, we evaluated *Klf6*, which was identified through our Taiji analysis as a T_{RM} single-state TF (Fig. 1g). We hypothesized whether overexpressing *Klf6* (*Klf6*-OE) would enhance T_{RM} formation during acute viral infection without worsen terminal exhaustion in chronic infection. Our results confirmed this hypothesis. When empty-vector control and *Klf6*-OE P14 CD8$^+$ T cells were co-transferred, *Klf6*-OE cells robustly outcompeted control cells, resulting in a 15-fold enrichment in the SI compared to controls (Fig. 4i). Furthermore, there were ~42 times more CD69$^+$ CD103$^+$double-

positive T_{RM}-like cells in *Klf6*-OE than in control donor cells, indicating *Klf6*-OE dramatically increased T_{RM} development in the SI (Fig. 4j). Importantly, *Klf6*-OE did not increase terminal exhaustion during chronic infection (Fig. 4k, Extended Data Fig. 7d). This work not only identified KLF6 as a new T_{RM}-driving TF but also confirmed its selectivity.

Novel TEX_{term}-TF loss improves tumor control

This platform predicted cell-state-selective TF activity and identified TEX_{term} single-state TFs as targets for engineering T cells that resist exhaustion yet retain effector and memory functions—offering new strategies to improve immunotherapy efficacy. Given that T_{RM} cells are associated with better clinical outcomes in solid tumors[9–12], we hypothesized that KO of exhaustion-selective TFs like *Zscan20* could be more effective than targeting T_{RM} and TEX_{term} multi-state TFs like *Hic1*. Utilizing an ACT model, TF gRNA RV-transduced Cas9$^+$ P14 CD8$^+$ T cells were transferred into mice with established melanoma tumors expressing GP33-41 (Fig. 5a). Unlike depletion of the multi-state TF *Hic1*, depleting the TEX_{term} single-state TF, *Zscan20*, resulted in improved tumor control (Fig. 5b,c). Moreover, *Zscan20* gRNA$^+$ cells more readily formed TEX_{prog} cells rather than TIM3$^+$ CD39$^+$ TEX_{term} cells (Fig. 5d,e). To control for inter-mouse variability in antigen load, we co-transferred *Zscan20* or *Hic1* KO with control P14 CD8$^+$ T cells into the same B16-GP33 tumor-bearing mice (Fig. 5f–j; Extended Data Fig. 8). Both KOs significantly increased the frequency of PD1$^+$ SLAMF6$^+$ TIM3$^-$ and decreased the frequency of TIM3$^+$ exhausted cells and TEX_{term} cell state (PD1$^+$ SLAMF6$^-$ CX3CR1$^-$) compared to controls (Extended Data Fig. 8), consistent with their predicted activity in TEX_{term} cells (Fig. 1f, h). However, *Zscan20* KO robustly enhanced effector marker expression (CX3CR1), granzyme B, and cytokine production in TILs, whereas *Hic1* KO did not appear to improve effector function to the same degree (Fig. 5g-j). Thus, despite their similar effects on suppressing TEX_{term} cell differentiation in tumors, differences in their ability to promote functional effector-like states may underlie the differential tumor control observed (Fig. 5b,c). Given that *Hic1* functions as a multi-state TF while *Zscan20* as a single-state TF, these findings support the general rationale for targeting state-specific TFs to enable more selective programming of T cell differentiation.

State-selective TFs conserved across species

To evaluate the relevance of our murine findings in human T cells—particularly for applications in immunotherapy—we conducted cross-species validation using publicly available single-cell multi-

omics and scRNA-seq datasets from human tumor-infiltrating $CD8^+$ T cells (Fig. 6a; Extended Data Fig. 9a; Supplementary Table 1). Leveraging the Taiji TF analysis platform, we mapped murine TEX_{term}- and T_{RM}-associated TFs onto a curated human pan-cancer $CD8^+$ T cell atlas encompassing six tumor types[49–56](GBM, HNSCC, BCC, HCC, RCC, and ccRCC). Human $CD8^+$ T cells were clustered into heterogeneous cell states, including T_{RM} and TEX_{term} clusters (Fig. 6a; Extended Data Fig. 9b). Taiji analysis revealed strong cross-species conservation: TEX_{term} TFs such as *JDP2*, *ZNF410*, and *FOXD2* exhibited higher activity in TEX_{term} clusters than in T_{RM}-like cells (Fig. 6b). Of 34 murine TEX_{term}-single-state TFs, 19 showed conserved activity patterns in human TEX_{term} cells. Similarly, T_{RM}-specific TF (e.g. *NR4A1*, *KLF6*, and *FOSB*) displayed enriched activity in the human T_{RM} cluster (Extended Data Fig. 9c). Furthermore, 22 of the 30 murine TFs active in both TEX_{term} and T_{RM} states showed similar activity profiles in human datasets (Extended Data Fig. 9d). A few TFs—such as ZSCAN20—could not be assessed in the Taiji analysis due to missing DNA-binding motifs, but comparative RNA profiling across 15 tumor types supported their relevance, with 24 of 34 murine 24 of 34 murine TEX_{term} single-state TFs, including *ZSCAN20* and *JDP2*, showing higher expression in human TEX cells.

Given these correlations between the species, we perturbed *ZSCAN20* and *JDP2* to assess the relevance of TEX_{term} single-state TFs in human T cells (Extended Data Fig. 10a,b). Following repeated CD3/CD28 stimulation over 18 days to simulate chronic activation (Fig. 6d), *ZSCAN20*- or *JDP2*-deficient $CD8^+$ T cells exhibited increased expression of CCR7 (naïve/stem cell memory/T_{CM} marker) and decreased levels of inhibitory receptors, including LAG3, PD1, and TIM3 (Fig. 6e, f). These KO cells also produced higher levels of effector cytokines and Granzyme B (Fig. 6g, h), indicating that ZSCAN20 and JDP2 contribute to exhaustion-associated features in human $CD8^+$ T cells.

ICB Synergy with *Zscan20* and *Jdp2* KOs

Tumors with high TEX_{term} cell infiltration often exhibit poor responses to immune checkpoint blockade therapy[17]. We hypothesized that targeting TEX_{term} single-state TFs could enhance ICB efficacy. Among the TEX_{term}-associated TFs, *Zscan20* and *Jdp2* were prioritized for their conservation and functional relevance in human T cells (Fig. 6b-h). To test synergy with ICB, treatment began one day after adoptive transfer of TF-depleted P14 $CD8^+$ T cells (Fig. 6i). The combination of *Zscan20* or *Jdp2* KO with anti-PD-1 therapy significantly reduced tumor burden (Fig. 6j–m) and improved survival (Extended Data Fig. 10c,d). These findings suggest that selectively disrupting TEX_{term} single-state TF represents a

promising strategy to enhance T cell therapy by minimizing dysfunctional states while preserving beneficial T cell phenotypes. Overall, our cross-species multi-omics and functional perturbation approach underscores the translational potential of Taiji-identified TFs for improving ACT.

Discussion

Our study introduces a powerful platform for identifying TFs pivotal in guiding specific $CD8^+$ T cell state differentiation during viral infections and tumor progression. Leveraging our comprehensive transcriptional/epigenetic atlas from nine distinct $CD8^+$ T cell states, we developed a detailed map of TF activity, creating a unique TF fingerprint for each context. Additionally, we developed TaijiChat, a web interface for natural language queries of our datasets and literature (Supplementary Method).

Focusing on two critical cell states TEX_{term} (dysfunctional terminally exhausted) and T_{RM} (functional, tissue-resident memory) T cells, we examined similarities and differences of TF activity and their networks in both states and engineered T cells to resist exhaustion while retaining functionality of T_{RM} cells. Using *in vivo* Perturb-seq, we validated TF activity for TEX_{term} and T_{RM} cells in both acute and chronic infection models. While recent CRISPR screenings in $CD8^+$ T cells have identified important TFs in cytotoxicity, memory formation[41–43], cell enrichment[57], and exhaustion[58], a systematic and context-dependent understanding of TF roles across multiple contexts has been lacking. Our study addresses this gap by generating an accurate catalogue of $CD8^+$ T cell state-defining TFs, enabling cost-effective validation of predicted TF activity and selectivity via Perturb-seq. Furthermore, our study offers broader and new insight into context-dependent TF regulation. Previously, differential TF cooperation in different contexts was reported[26,43,44]. We extend this by analyzing global TF associations across cell states, revealing how TF communities regulate T cell-specific pathways, including protein catabolism in T cell exhaustion, which aligns with prior research on protein homeostasis[46,59,60]. These TF networks reveal how various cellular processes are differentially controlled between T_{RM} and TEX_{term} cells, providing rationale for their different functional capabilities within tissues.

One of the key outcomes of this study was the identification of novel TFs, including ZSCAN20 and JDP2 as TEX_{term} single-state TFs, KLF6 as a T_{RM} single-state TF, and newly uncovered roles for multi-state TFs such as HIC1 and GFI1. Perturbing TEX_{term} single-state TFs not only prevented T cell exhaustion but also preserved the ability of these cells to differentiate into effector and memory states. This led to significant improvements in tumor control.

To evaluate the clinical importance of the newly discovered TFs and the catalog of TFs with TEX_{term} and T_{RM} selectivity, we confirmed cross-species conservation of a significant number of TFs using Taiji analysis of a human pan-cancer multi-omics atlas, along with comparative expression analysis across pan-cancer single-cell RNA-seq datasets. Furthermore, we demonstrated enhanced human T cell function following perturbation of the TEX_{term} single-state TFs *ZSCAN20* and *JDP2*. Depletion of these TFs shows synergistic effects with ICB therapy, leading to significant tumor regression. These findings highlight a promising strategy for enhancing antitumor immunity through precise cell-state programming.

Our TF atlas-guided platform can offer optimized 'TF recipes' for cell programming with increased precision, robustness, and durability. Future strategies may combine overexpression of T_{RM} -promoting TFs like KLF6 with depletion of TEX_{term} TFs. Such recipes can be refined with AI models. In summary, while our study focuses on $CD8^+$ TEX_{term} and T_{RM} cell differentiation, the pipeline for identifying single-state TFs and 'TF recipes' can be adapted for other cell types, expanding cell therapy applications.

References

1. Chung, H. K., McDonald, B. & Kaech, S. M. The architectural design of CD8+ T cell responses in acute and chronic infection: Parallel structures with divergent fates. *J. Exp. Med.* **218**, (2021).
2. Kasmani, M. Y. *et al.* Clonal lineage tracing reveals mechanisms skewing CD8+ T cell fate decisions in chronic infection. *J. Exp. Med.* **220**, (2023).
3. Beltra, J.-C. *et al.* Developmental Relationships of Four Exhausted CD8 T Cell Subsets Reveals Underlying Transcriptional and Epigenetic Landscape Control Mechanisms. *Immunity* **52**, 825–841.e8 (2020).
4. Giles, J. R. *et al.* Shared and distinct biological circuits in effector, memory and exhausted CD8 T cells revealed by temporal single-cell transcriptomics and epigenetics. *Nature Immunology* vol. 23 1600–1613 Preprint at https://doi.org/10.1038/s41590-022-01338-4 (2022).
5. Pauken, K. E. *et al.* Epigenetic stability of exhausted T cells limits durability of reinvigoration by PD-1 blockade. *Science* **354**, 1160–1165 (2016).
6. Sen, D. R. *et al.* The epigenetic landscape of T cell exhaustion. *Science* vol. 354 1165–1169 Preprint at https://doi.org/10.1126/science.aae0491 (2016).
7. Wherry, E. J., Blattman, J. N., Murali-Krishna, K., van der Most, R. & Ahmed, R. Viral persistence alters CD8 T-cell immunodominance and tissue distribution and results in distinct stages of functional impairment. *J. Virol.* **77**, 4911–4927 (2003).
8. Wherry, E. J. *et al.* Molecular signature of CD8+ T cell exhaustion during chronic viral infection. *Immunity* **27**, 670–684 (2007).
9. Milner, J. J. *et al.* Runx3 programs CD8 T cell residency in non-lymphoid tissues and tumours. *Nature* **552**, 253–257 (2017).
10. Ganesan, A.-P. *et al.* Tissue-resident memory features are linked to the magnitude of cytotoxic T cell responses in human lung cancer. *Nat. Immunol.* **18**, 940–950 (2017).
11. Djenidi, F. *et al.* CD8 CD103 Tumor–Infiltrating Lymphocytes Are Tumor-Specific Tissue-Resident Memory T Cells and a Prognostic Factor for Survival in Lung Cancer Patients. *The Journal of Immunology* vol. 194 3475–3486 Preprint at https://doi.org/10.4049/jimmunol.1402711 (2015).
12. Corgnac, S., Boutet, M., Kfoury, M., Naltet, C. & Mami-Chouaib, F. The Emerging Role of CD8+ Tissue Resident Memory T (TRM) Cells in Antitumor Immunity: A Unique Functional Contribution of the CD103 Integrin. *Front. Immunol.* **9**, 1904 (2018).
13. Komdeur, F. L. *et al.* CD103+ tumor-infiltrating lymphocytes are tumor-reactive intraepithelial

CD8+ T cells associated with prognostic benefit and therapy response in cervical cancer. *Oncoimmunology* **6**, e1338230 (2017).

14. Kaech, S. M. & Cui, W. Transcriptional control of effector and memory CD8+ T cell differentiation. *Nat. Rev. Immunol.* **12**, 749–761 (2012).

15. Sen, D. R. *et al.* The epigenetic landscape of T cell exhaustion. *Science* vol. 354 1165–1169 Preprint at https://doi.org/10.1126/science.aae0491 (2016).

16. Im, S. J. *et al.* Defining CD8+ T cells that provide the proliferative burst after PD-1 therapy. *Nature* **537**, 417–421 (2016).

17. Miller, B. C. *et al.* Subsets of exhausted CD8 T cells differentially mediate tumor control and respond to checkpoint blockade. *Nat. Immunol.* **20**, 326–336 (2019).

18. Hudson, W. H. *et al.* Proliferating Transitory T Cells with an Effector-like Transcriptional Signature Emerge from PD-1 Stem-like CD8 T Cells during Chronic Infection. *Immunity* **51**, 1043–1058.e4 (2019).

19. Liu, F. *et al.* CTLA-4 correlates with immune and clinical characteristics of glioma. *Cancer Cell Int.* **20**, 7 (2020).

20. Zhang, M. *et al.* Prognostic Values of CD38+CD101+PD1+CD8+ T Cells in Pancreatic Cancer. *Immunol. Invest.* (2019) doi:10.1080/08820139.2019.1566356.

21. Shin, H. *et al.* A role for the transcriptional repressor Blimp-1 in CD8(+) T cell exhaustion during chronic viral infection. *Immunity* **31**, 309–320 (2009).

22. Behr, F. M. *et al.* Blimp-1 Rather Than Hobit Drives the Formation of Tissue-Resident Memory CD8 T Cells in the Lungs. *Front. Immunol.* **10**, 400 (2019).

23. Milner, J. J. *et al.* Heterogenous Populations of Tissue-Resident CD8+ T Cells Are Generated in Response to Infection and Malignancy. *Immunity* **52**, 808–824.e7 (2020).

24. Li, C. *et al.* The Transcription Factor Bhlhe40 Programs Mitochondrial Regulation of Resident CD8 T Cell Fitness and Functionality. *Immunity* **51**, 491–507.e7 (2019).

25. Wu, J. E. *et al.* In vitro modeling of CD8 T cell exhaustion enables CRISPR screening to reveal a role for BHLHE40. *Sci Immunol* **8**, eade3369 (2023).

26. Chen, J. *et al.* NR4A transcription factors limit CAR T cell function in solid tumours. *Nature* **567**, 530–534 (2019).

27. Mackay, L. K. *et al.* The developmental pathway for CD103(+)CD8+ tissue-resident memory T cells of skin. *Nat. Immunol.* **14**, 1294–1301 (2013).

28. Schacht, T., Oswald, M., Eils, R., Eichmüller, S. B. & König, R. Estimating the activity of transcription factors by the effect on their target genes. *Bioinformatics* **30**, i401–7 (2014).

29. Zhang, K., Wang, M., Zhao, Y. & Wang, W. Taiji: System-level identification of key transcription factors reveals transcriptional waves in mouse embryonic development. *Sci Adv* **5**, eaav3262 (2019).

30. Wang, J., Liu, C., Chen, Y. & Wang, W. Taiji-reprogram: a framework to uncover cell-type specific regulators and predict cellular reprogramming cocktails. *NAR Genom Bioinform* **3**, lqab100 (2021).

31. Liu, C. *et al.* Systems-level identification of key transcription factors in immune cell specification. *PLoS Comput. Biol.* **18**, e1010116 (2022).

32. Milner, J. J. *et al.* Delineation of a molecularly distinct terminally differentiated memory CD8 T cell population. *Proc. Natl. Acad. Sci. U. S. A.* **117**, 25667–25678 (2020).

33. Guan, T. *et al.* ZEB1, ZEB2, and the miR-200 family form a counterregulatory network to regulate CD8 T cell fates. *J Exp Med* **215**, 1153–1168 (2018).

34. Scott-Browne, J. P. *et al.* Dynamic Changes in Chromatin Accessibility Occur in CD8 T Cells Responding to Viral Infection. *Immunity* **45**, 1327–1340 (2016).

35. Mackay, L. K. *et al.* Hobit and Blimp1 instruct a universal transcriptional program of tissue residency in lymphocytes. *Science* **352**, 459–463 (2016).

36. Renkema, K. R. *et al.* KLRG1 Memory CD8 T Cells Combine Properties of Short-Lived Effectors and Long-Lived Memory. *J Immunol* **205**, 1059–1069 (2020).

37. Intlekofer, A. M. *et al.* Effector and memory CD8+ T cell fate coupled by T-bet and eomesodermin. *Nat Immunol* **6**, 1236–1244 (2005).

38. Reiser, J., Sadashivaiah, K., Furusawa, A., Banerjee, A. & Singh, N. Eomesodermin driven IL-10 production in effector CD8 T cells promotes a memory phenotype. *Cell Immunol* **335**, 93–102 (2019).

39. Crowl, J. T. *et al.* Tissue-resident memory CD8 T cells possess unique transcriptional, epigenetic and functional adaptations to different tissue environments. *Nature Immunology* vol. 23 1121–1131 Preprint at https://doi.org/10.1038/s41590-022-01229-8 (2022).

40. Chandele, A. *et al.* Formation of IL-7Ralphahigh and IL-7Ralphalow CD8 T cells during infection is regulated by the opposing functions of GABPalpha and Gfi-1. *J. Immunol.* **180**, 5309–5319 (2008).

41. Schmidt, R. *et al.* CRISPR activation and interference screens decode stimulation responses in primary human T cells. *Science* **375**, eabj4008 (2022).

42. Shifrut, E. *et al.* Genome-wide CRISPR Screens in Primary Human T Cells Reveal Key Regulators of Immune Function. *Cell* **175**, 1958–1971.e15 (2018).

43. McCutcheon, S. R. *et al.* Transcriptional and epigenetic regulators of human CD8+ T cell function identified through orthogonal CRISPR screens. *Nat. Genet.* **55**, 2211–2223 (2023).

44. Seo, H. *et al.* BATF and IRF4 cooperate to counter exhaustion in tumor-infiltrating CAR T cells. *Nat. Immunol.* **22**, 983–995 (2021).

45. Guo, X. *et al.* Global characterization of T cells in non-small-cell lung cancer by single-cell sequencing. *Nat Med* **24**, 978–985 (2018).

46. Riesenberg, B. P. *et al.* Stress-Mediated Attenuation of Translation Undermines T-cell Activity in Cancer. *Cancer Res.* **82**, 4386–4399 (2022).

47. Daniel, B. *et al.* Divergent clonal differentiation trajectories of T cell exhaustion. *Nat. Immunol.* **23**, 1614–1627 (2022).

48. Lin, Y. H. *et al.* Small intestine and colon tissue-resident memory CD8+ T cells exhibit molecular heterogeneity and differential dependence on Eomes. *Immunity* **56**, 207–223.e8 (2023).

49. Long, Z. *et al.* Single-cell multiomics analysis reveals regulatory programs in clear cell renal cell carcinoma. *Cell Discov* **8**, 68 (2022).

50. Terekhanova, N. V. *et al.* Epigenetic regulation during cancer transitions across 11 tumour types. *Nature* **623**, 432–441 (2023).

51. Riegel, D. *et al.* Integrated single-cell profiling dissects cell-state-specific enhancer landscapes of human tumor-infiltrating CD8 T cells. *Mol Cell* **83**, 622–636.e10 (2023).

52. Yost, K. E. *et al.* Clonal replacement of tumor-specific T cells following PD-1 blockade. *Nat Med* **25**, 1251–1259 (2019).

53. Ma, L. *et al.* Tumor Cell Biodiversity Drives Microenvironmental Reprogramming in Liver Cancer. *Cancer Cell* **36**, 418–430.e6 (2019).

54. Young, M. D. *et al.* Single-cell transcriptomes from human kidneys reveal the cellular identity of renal tumors. *Science* **361**, 594–599 (2018).

55. Cillo, A. R. *et al.* Immune Landscape of Viral- and Carcinogen-Driven Head and Neck Cancer. *Immunity* **52**, 183–199.e9 (2020).

56. Zheng, L. *et al.* Pan-cancer single-cell landscape of tumor-infiltrating T cells. *Science* **374**,

abe6474 (2021).

57. Chen, Z. *et al.* In vivo CD8+ T cell CRISPR screening reveals control by Fli1 in infection and cancer. *Cell* **184**, 1262–1280.e22 (2021).

58. Zhou, P. *et al.* Single-cell CRISPR screens in vivo map T cell fate regulomes in cancer. *Nature* **624**, 154–163 (2023).

59. Van Der Byl, W. *et al.* The CD8+ T cell tolerance checkpoint triggers a distinct differentiation state defined by protein translation defects. *Immunity* (2024) doi:10.1016/j.immuni.2024.04.026.

60. Chang, J. T. *et al.* Asymmetric proteasome segregation as a mechanism for unequal partitioning of the transcription factor T-bet during T lymphocyte division. *Immunity* **34**, 492–504 (2011).

Figure Legends

Fig. 1| Transcriptional and epigenomic atlas of CD8$^+$ T cell differentiation states and TF identification pipeline. a, Diagram summarizing CD8$^+$ T cell trajectories during acute and chronic infection or tumor, highlighting differentiation into various effector, memory, and exhaustion states, including parallel TRM and TEXterm lineages with overlapping tissue localization. **b,** Pearson correlation matrix of batch-effect–corrected RNA-seq datasets. Both color intensity and circle size indicate correlation strength, with red denoting the highest correlation. **c,** Workflow of the integrative Taiji analysis. Matched RNA-seq and ATAC-seq datasets[3,9,18,23,32–36] were used to construct a regulatory network and calculate TF activity scores using PageRank. Downstream analysis included identification of single- and multi-state TFs, TF "waves" and network communities. **d-h,** TFs (rows) and samples (columns) are displayed as z-normalized PageRank heatmaps. Each column corresponds to a dataset. **d,** PageRank scores of 136 single-state TFs. **e,** 173 multi-state TFs. **f-h**, Bubble plots show normalized TF PageRank scores and expression for TEX_{term}-selective **(f),** T_{RM} -selective **(g),** and multi-state **(h)** TFs active in both cell states. TEX_{term} single-state TFs are bolded. Circle color represents the normalized PageRank score (red = high), and circle size indicates log mRNA expression across five datasets. TFs are ordered by *P* value; validated TFs are highlighted in gray. **i-j,** TF "waves" associated with exhaustion **(i)** or T_{RM} differentiation **(j)**, indicating coordinated activity of TF groups during cell state transistions. Sample sizes and statistical details for cell state definitions and TF selection criteria are provided in Extended Data Fig. 1e and Extended Data Fig. 2a, respectively.

Fig. 2| Global analysis of TF networks in TEX_{term} and T_{RM} cell states. a, Overview of TF–TF network analysis encompassing association and community-level organization of TRM and TEXterm regulatory landscapes. **b-c,** TF-TF association networks focused on the TEX_{term} single-state TF ZSCAN20 **(b)** and the multi-state TF HIC1 **(c)**, depicting predicted context-specific interactions in T_{RM} (green) or TEX_{term} (brown) cells. **d-f,** Clustering of TF–TF associations identified five distinct TF communities in TRM and TEXterm networks. Shared TFs (gray) shape overall community topology **(d),** whereas T_{RM}- or TEX_{term}-specific interactions are represented as green **(e)** or brown **(f)** edges, respectively. **g,** Summary of shared and unique biological pathways enriched within T_{RM} and TEX_{term} communities. Line thickness reflects $-log_{10}(P$ value). (Pathway gene sets in Supplementary Table 8). **h**, Gene set enrichment analysis (GSEA) comparing TEX_{term} vs. T_{RM} cell pathways using batch-effect corrected LCMV bulk-RNA-seq[3,9,18,23,32–36] and human pan-cancer scRNA-seq data sets[45,56,61]. **i-k,** Flow cytometry analysis of

proteasome activity showing the highest activity in TEX_{term} cells during LCMV-Clone 13 infection **(i)** and MCA-205 tumors **(j).** In dual transfer experiments, antigen-specific (P14) and bystander (OT-1) $CD8^+$ T cells analyzed from B16-GP33 tumors **(k)** show elevate proteasome activity in TEX_{term}-like populations. **l,** Functional impact of proteasome activity on tumor growth. Tumor-bearing C57BL/6 mice infused with $proteasome^{high}$ or $proteasome^{low}$ OT-1 cells pre-stimulated with B16F1-OVA tumor cells for seven days. $Proteasome^{high}$ OT-1 cells exhibit reduced tumor control. Data are shown as the mean ±s.e.m. Ordinary one-way ANOVA **(i-k),** and two-way ANOVA Tukey's multiple comparison test **(l)** were performed. ****P<0.0001, ***P<0.001, **P<0.01, *P<0.05.

Fig. 3| *In vivo* Perturb-seq validation of TEX_{term}-driving TFs. a, Schematic of the *in vivo* Perturb-seq strategy. $Cas9^+$ $P14^+$ TCR-transgenic $CD8^+$ T cells recognizing LCMV epitope GP33-41 epitope were transduced with retroviruses (RVs) expressing gRNA libraries, adoptively transferred into mice previously infected one day earlier with LCMV-Clone 13, and analyzed 18-23 days later by scRNA-seq. **b**, UMAP showing TEX_{prog}, TEX_{eff}, TEX_{term}, and cell cycle clusters; marker expression are in Extended Data Fig. 6b,c. **c-d**, Kernel density plots and distributions of $gRNA^+$ cells across clusters. TEX_{term} single-state TFs are indicated bolded. Data represent five pooled replicates from three independent experiments; values are shown as mean ± s.e.m. Statistical analysis: two-way ANOVA with Fisher's LSD test compared to the gScramble control; results for TEX_{term} and TEX_{prog} clusters are shown; with full comparisons in Supplementary Table 7. ****P < 0.0001, ***P < 0.001, **P < 0.01, *P < 0.05. **e**, Representative flow plots showing phenotyping of the TF knockouts (Kos) in LCMV-Clone 13-infected mice. **f**, Quantification of TEX_{term} ($PD1^+$ $SLAMF6^-$ $CX3CR1^-$) frequencies in donor $CD8^+$ T cells. **g**, Differential expression analysis of TEX_{term}, TEX_{prog}, and TEX_{eff} gene signatures (ref. [47]; Supplementary Table 8) across each TF KO. **h-i**, Frequencies of TEX_{prog} ($PD1^+$ $SLAMF6^+$ $CX3CR1^-$) and TEX_{eff} ($PD1^+$ $CX3CR1^+$) subsets. **j**, GSEA showing enrichof effector-associated gene sets in TF KOs *vs*. control. **k-l**, Functional validation: cytokine production (IFNγ, TNFα) and viral titers in mice receiving TF KO versus control $CD8^+$ T cells. Statistic analysis for **f, h, i, k, l**: mean ± s.e.m., ordinary one-way ANOVA with Dunnett's multiple comparison versus gScramble (**f-k**: n ≥ 8, ≥ 3 biological replicates, **i**: n ≥ 4, ≥ 2 biological replicates). ***P<0.001, ** P <0.01, * P <0.05.

Fig. 4| Functional validation of TFs with distinct roles in TEX_{term} and TRM differentiation. a, Schematic of *in vivo* Perturb-seq screening during acute LCMV-Armstrong infection to assess memory $CD8^+$ T cell differentiation. Transduced donor $Cas9^+$ $P14^+$ $CD8^+$ T cells were analyzed for tissue-

resident (T_{RM}), effector-memory (T_{EM}), and central-memory (T_{CM}) states in the small intestine (SI) and spleen. **b,** UMAP embedding of 15,211 cells identifying T_{CM} (*Il7r*, *Tcf7*, *Sell*, *S1pr1*), T_{EM} (*Cx3cr1*, *Klrg1*, *Klf2*), T_{RM} (*Cd69*, *Itgae*, *Cd160*), and T_{RM}- *Itgae*^{low} clusters. **c,** Differential distribution of cells across tissues. **d,** Kernel-density map of gRNA$^+$ cells in UMAP space. **e,** Cluster distribution for each TF gRNA; TEX_{term} single-state TFs in bold. Data represent three replicates; mean ± s.e.m. Statistical analysis: two-way ANOVA with Fisher's LSD versus gScramble. ****P < 0.0001, ***P < 0.001, **P < 0.01, *P < 0.05; details in Supplementary Table 5. **f,** Normalized expression of T_{RM} "up" and "down" gene-signatures[9,35] in each KO versus control. **g-h,** Phenotypic validation: **(g)**, ratio of gRNA$^+$ cells in SI to spleen and **(h)**, frequency of splenic T_{CM} (CD62L$^+$ KLRG1$^-$) and T_{EM} (CD62L$^-$ KLRG1$^+$) cells. **i-j,** T_{RM} single-state TF, *Klf6* OE enhances T_{RM} formation. P14$^+$ CD8$^+$ T cells transduced with *Klf6* or empty-vector were co-transferred (~1:1) into LCMV-Armstrong-infected mice. **i,** Representative plots pre- and post-transfer. **j,** Quantification of donor CD69$^+$ CD103$^+$ T_{RM} cells in the SI. **k**. Quantification of the frequency of TEX_{term} cells. Statistical tests: ordinary one-way ANOVA with Dunnett's multiple comparison versus gScramble (**g-h**), paired t-tests (**i-j**). n ≥ 4 (**g-h**) or n ≥ 6 (**i-k**) from ≥ 2 biological replicates. Data mean ± s.e.m. ***P<0.001, ** P <0.01, * P <0.05

Fig. 5 | Distinct roles of TEX_{term} single-state TF *Zscan20* and multi-state TF *Hic1* in tumor control. **a**, Experimental design: adoptive transfer of P14 CD8$^+$ T cells with CRISPR KOs of either *Zscan20* (TEX_{term} single-state TF) or a *Hic1* (multi-state TF active in TEX_{term} and T_{RM}) into B16-GP33 melanoma-bearing mice. **b-c**, Tumor volumes **(b)** and terminal weights **(c)** at day 23. **d**, Representative flow plots of PD1$^+$ P14 cells stained for SLAMF6 and TIM3, with quantification of TEX_{prog} (PD1$^+$ SLAMF6$^+$ TIM3$^-$) and exhausted (PD1$^+$ SLAMF6$^-$ TIM3$^+$) subsets. **e**, Frequency of PD1$^+$ CD39$^+$ double-positive cells. **f-j**, Co-transfer design **(f)** mixing *Zscan20*- or *Hic1*-KO Cas9$^+$ P14 cells with scramble-control cells before transfer. **g**, Representative plots of effector marker CX3CR1$^+$ and cytotoxic cytokine GzmB in TF KO versus control. **h-j**, Quantification of CX3CR1$^+$ (**h**), GzmB$^+$ (**i**), and polyfunctional IFNγ$^+$ TNFα$^+$ (**j**) cells in *Zscan20* (left) or *Hic1* (right) KOs. Data represent n ≥ 8 (**b–e**) and n ≥ 6 (**g–j**) from ≥ 2 biological replicates. Statistical analysis: two-way ANOVA with Tukey's multiple comparisons (**b**), one-way ANOVA with Dunnett's test versus gScramble (**c**), paired t-tests (**g-j**). Data mean ± s.e.m. ****P < 0.0001, ***P < 0.001, **P < 0.01, *P < 0.05.

Fig. 6 | Targeting conserved TEX_{term} single-state TFs enhances human T cell effector function and ICB response

a, Human pan-cancer single-cell multi-omics and scRNA-seq datasets[49–56] were integrated to evaluate TF expression and activity across $CD8^+$ T cell states using the scTaiji algorithm. **b**, Paired scRNA-seq and scATAC-seq data were used to construct regulatory networks and compute PageRank TF activity scores. Shown are normalized scores of TEX_{term} single-state TFs (Fig. 1f) with conserved DNA-binding motifs in the human genome. **c,** mRNA expression of TEX_{term} TFs across TEX_{term} and TRM clusters in pan-cancer datasets; TFs with cross-species conservation in bold. **d,** Experimental design for human PBMC TF KOs. *ZSCAN20*- or *JDP2*-KO $CD8^+$ T cells were stimulated with anti-CD3/CD28 beads for 18 days to model chronic activation. **e-f,** Flow cytometry analysis of CCR7 (memory/stem-like) and inhibitory receptors LAG3, PD1, TIM3 in KO versus control cells. **g,** Frequency of $IFN\gamma^+$ $TNF\alpha^+$ and and IL-2 cells. **h,** Polyfunctionality analysis of cytokine-producing cells. **i,** Schematic of adoptive transfer and anti–PD-1 therapy to test synergy with TEXterm TF KO. $Cas9^+$ P14 cells (with or without TF KO) were transferred into B16-GP33 tumor-bearing mice and treated with anti–PD-1 or isotype IgG2a. **j–m,** Tumor growth and weights of *Zscan20* (**j-k**) and *Jdp2* (**l–m)** KO versus controls. Data: mean ± s.e.m.; n ≥ 6 from ≥2 biological replicates. One-way ANOVA with Dunnett's test (**e-g**); two-way ANOVA with Dunnett's (**h**) or Tukey's (**j,l**), and one-way ANOVA with Tukey's (**k, m**). ****P < 0.0001, ***P < 0.001, **P < 0.01, *P < 0.05.

Methods

Dataset acquisition for murine CD8$^+$ T cell state multiomics atlas: CD8$^+$ T cell samples were collected from ten datasets, including those generated in this study (Extended Data Fig. 1e). In total, we analyzed 121 experiments, comprising 52 ATAC-seq and 69 RNA-seq datasets, which were integrated to generate paired samples and served as input for the Taiji pipeline. The samples encompassed nine distinct CD8$^+$ T cell subtypes: naive cells (Naive), terminal effector cells (TE), memory precursor cells (MP), tissue-resident memory cells (T_{RM}), effector memory cells (T_{EM}), central memory cells (T_{CM}), progenitor exhausted cells (TEX_{prog}), intermediate exhausted cells (TEX_{eff}) and terminal exhausted cells (TEX_{term}). Cell states were defined based on established surface marker combinations and LCMV (lymphocytic choriomeningitis virus)-specific tetramers, including IL7R, KLRG1, PD1, SLAMF6, CD101, Tim3, CD69, CD103, H2-Db LCMV gp 33-41 and H2-Db LCMV gp 276-286 or congenic markers for P14 (T cell receptor (TCR) specific for the LCMV GP33–41 peptide CD8$^+$ T cells), in the context of either acute (LCMV-Armstrong) or chronic (LCMV-Clone 13) infection models. A complete summary of dataset sources, accession numbers, infection conditions, and corresponding cell state definitions (sorting gates) is provided in Supplementary Table 1 and Extended Data Fig. 1e.

TF regulatory networks construction and visualization: To perform integrative analysis of RNA-seq and ATAC-seq data, we developed Taiji v2.0. which allows visualization of several downstream analysis-TF wave, TF-TF association, TF community analysis. Epitensor was used for the prediction of chromatin interactions. Putative TF binding motifs were curated from the latest CIS-BP database[62]. In this analysis, 695 TFs were identified as having binding sites centered around ATAC-seq peak summits. The average number of nodes (genes) and edges (interactions) of the genetic regulatory networks across CD8$^+$ T cell states were 15,845 and 1,325,694, respectively, including 695 (4.38%) TF nodes. On average, each TF regulated 1,907 genes, and each gene was regulated by 22 TFs.

Identification of single-state/multi-state TFs: We first identified universal TFs with mean PageRank across 9 cell states ranked as top 10% and Coefficients of variation (CV) less than 0.5. In total, 54 universal TFs were identified and shown in Supplementary Table 1. The remaining 641 TFs were candidate TFs for single-state TFs. To identify single-state TFs, we divided the samples into two groups: target group and background group. Target group included all the samples belonging to the cell state of interest and the background group comprised the remaining samples. We then performed the normality

test using Shapiro-Wilk's method to determine whether the two groups were normally distributed, and we found that the PageRank scores of most samples (90%) follow a log-normal distribution. Based on the log-normality assumption, an unpaired t-test was used to calculate the P-value. A P-value cutoff of 0.05 and log2 fold change cutoff of 0.5 were used for calling lineage-specific TFs In total, 255 specific TFs were identified (Supplementary Table 2). Depending on whether the TF appeared in multiple cell states, they could be further divided into multi-state TFs (Supplementary Table 2, Fig 1e) and 136 single-state exclusive TFs (Supplementary Table 2, Fig. 1d). Out of 255 single-state TFs, 84 TFs appear in TEX_{term} or T_{RM}. To identify the truly distinctive TFs between TEX_{term} and T_{RM}, we performed a second round of unpaired t-test only between TEX_{term} and T_{RM} (Supplementary Table 3). The same cut-offs, i.e. P-value of 0.05 and log2 fold change of 0.5, were applied to select TEX_{term} single-taskers and T_{RM} single-taskers. Thirty out of 84 TFs that did not pass the cut-off were identified as TEX_{term} and T_{RM} multi-taskers. The full workflow was summarized in Extended Data Fig. 2a.

Identification of transcriptional waves: Combined with prior knowledge on the T cell differentiation path, TF waves are combinations of TFs which are particularly active in certain differentiation stages, revealing possible mechanisms of how TF activities are coordinated during differentiation. To be more specific, we clustered the TFs based on the normalized PageRank scores across samples. First, we performed principal component analysis (PCA) for dimensionality reduction of the TF score matrix. We retained the first 10 principal components for further clustering analysis, which explained more than 70% variance (Extended Data Fig. 3b; left panel). We used the k-means algorithm for clustering analysis. To find the optimal number of clusters and similarity metric, we performed the Silhouette analysis to evaluate the clustering quality using five distance metrics: Euclidean distance, Manhattan distance, Kendall correlation, Pearson correlation, and Spearman correlation (Extended Data Fig. 3b; right panel). Pearson correlation was the most appropriate distance metric since the average Silhouette width was the highest among all five distance metrics. Based on these analyses, we identified 7 distinct dynamic patterns of TF activity during immune cell development. We further performed functional enrichment analysis to identify GO terms for these clusters.

TF-TF collaboration network analysis and visualization: To build the TF-TF association networks, we first defined a set of relevant TFs for each context (TEX_{term} and T_{RM}) by combining cell state-important and single-state TFs, resulting in 159 TFs for TEX_{term} and 170 for T_{RM}. The analysis was

based on a TF-regulatee network derived from Taiji, where we first consolidated sample networks by averaging the edge weights for each TF-regulatee pair. To reduce noise, regulatees with low variation across all TFs (standard deviation ≤ 1) were removed. Subsequently, a TF-TF correlation matrix was generated by calculating the Spearman's correlation of edge weights for each TF pair across their common regulatees. From this matrix, we constructed a graphical model using the R package "huge"[63], which employs the Graphical Lasso algorithm and a shrunken ECDF (empirical cumulative distribution function) estimator. An edge between two TFs was established if their correlation was deemed significant by the model, controlled by a lasso penalty parameter (lambda) of 0.052. This value was chosen as it represents a local minimum on the sparsity-lambda curve, resulting in approximately 15% of TF-TF pairs being connected. To validate this method, we estimated the false discovery rate by generating a null model through random shuffling of the TF-regulatee edge weights. Applying our algorithm to this null data identified zero interactions, confirming that our approach has a very low false discovery rate.

TF community construction and visualization: Following the construction of the TF-TF association networks, we identified functionally related TF communities within each network. We applied the Leiden algorithm[64], using modularity as the objective function and setting the resolution parameter to 0.9, as this value achieved the highest clustering modularity in our analysis. This procedure identified five distinct communities for each context (TEX_{term} and T_{RM}). The final networks, with their detected communities, were visualized using the Fruchterman-Reingold layout algorithm[65] to spatially represent the TF-TF association structure.

Pathway enrichment analysis: The enriched functional terms in this study were analyzed by the R package clusterProfiler 4.0.5. We used GO, KEGG, MSigDb databases for annotation. For gene set enrichment analysis (GSEA), the genes were first ranked by the mean edge weight in corresponding samples and H, C5, C6, and C7 collections from MSigDb were used for annotation. A cutoff of P-value < 0.05 was used to select the significantly enriched GO terms and KEGG pathways.

Heuristic score calculation via the integration of TF regulatory network and Perturb-seq:
We reasoned that (1) log2FC change in expression due to TF KO, and (2) TF-gene regulatory edge weights could be combined to provide heuristic scores for a TF's regulatory effect on a target gene. For

each guide RNA KO, Seurat's FindMarkers() function was used to quantify log2FC of gene's expression with respect to the gScramble condition. Heuristic scores were calculated for each TF-gene pair by multiplying the gene log2FC with the corresponding edge weight from the Taiji analysis. Regulatees of a TF were annotated as high-confidence if the magnitude log2FC of the regulate exceeded 0.58 (corresponding to a fold-change of 1.5 or its reciprocal) and if the edge weight belonged to the upper quantile of all edge weights attributed to the TF. The sign of the log2FC was used to determine if the TF activated or repressed each target gene.

Human TF activity and cell-state selectivity analysis:

Taiji-based analysis of human multiomic datasets. Transcription factor (TF) activity was inferred using the Taiji pipeline applied to matched single-cell RNA-seq (scRNA-seq) and ATAC-seq (scATAC-seq) datasets from various human cancers, including ccRCC (n=2; PRJNA768891, GSE240822), GBM (GSE240822), BCC (GSE123814, EGAS00001006141), HNSCC (GSE139324, EGAS00001006141), HCC (GSE125449, EGAS00001006141), and RCC (PMID: 30093597; EGAS00001006141). Cell types were annotated using canonical marker gene expression and categorized into six major CD8+ T cell states: T_Ex (exhausted), T_ExProg (progenitor exhausted), T_Eff (effector), T_RM (tissue-resident memory), T_CM/Naive (central memory/naive), and proliferating. PageRank scores derived from Taiji were log-transformed, averaged within each T cell category, and then standardized using z-score normalization. Results were visualized with a focus on TF activity in T_RM and T_Ex populations.

TF expression comparison across human CD8+ T cell states. To assess TF expression across diverse T cell states, raw count matrices from a published pan-cancer CD8+ T cell atlas (GSE156728) were reprocessed using Seurat's standard workflow. The dataset encompassed T cells from 11 tumor types, including BC, BCL, CHOL, ESCA, FTC, MM, OV, PACA, RC, THCA, and UCEC. Cell type annotations provided by the original study were retained and mapped to the following broad categories: T_RM, T_Ex, T_EM (effector memory), T_m (memory), T_n (naive), and T_k (cycling). Seurat's AverageExpression function was used to compute average logCPM expression for each TF in each T cell category, followed by z-score normalization. Data visualization emphasized comparisons between T_RM and T_Ex subsets.

Mice and infections: C57BL/6/J, OT-1 (C57BL/6-Tg(TcraTcrb)1100Mjb/J), B6.Cg-*Rag2*$^{tm1.1Cgn}$/J, CD45.1 (B6.SJL-*PtprcaPepcb*/BoyJ) mice were purchased from Jackson Laboratories. P14 mice (Pircher et al., 1987) mice have been previously described. Cas9 P14 mice were generated by crossing P14 mice with B6(C)-Gt(ROSA)26Sorem1.1(CAG-cas9*,-EGFP)Rsky/J (Jackson Laboratories). Animals were housed in specific-pathogen-free facilities at the Salk Institute and University and at the University of North Carolina at Chapel Hill. All animal experiments were approved by the Institutional Animal Care and Use Committee (IACUC). Mice were infected with $2x10^5$ PFU LCMV-Armstrong by intraperitoneal injection or $2x10^6$ PFU LCMV-Clone13 by retro-orbital injection under anesthesia.

Viral titers: LCMV Fluorescence Focus Unit titration was performed seeding Vero cells at a density of 30k cells/100µl in a 96 well flat bottom plate in DMEM + 10% FBS + 2% HEPES + 1% Pen/Strep. On the next day, tissues were homogenized on ice, spun down at 1000g for 5 min at 4°C and supernatants or serum were diluted in 10-fold steps. Diluted samples were added to Vero cells and incubated at 37°C, 5% CO_2 for ~20h. Subsequently, inocula were aspirated and wells were incubated with 4% PFA for 30 min at RT before washing with PBS. VL-4 antibody (BioXCell) was conjugated using the Invitrogen AF488 conjugation kit and added to the wells in dilution buffer containing 3% BSA and 0.3% Triton (Thermo Fisher Scientific) in PBS. Cells were incubated at 4°C overnight before washing with PBS and counting foci under the microscope. FFU was calculated per this formula: FFU/ml=Number of plaques/ (dilution× volume of diluted virus added to the plate).

Cell isolation: Spleens were mechanically dissociated with 1mL syringe plungers over a 70um nylon strainer. Spleens were incubated in ammonium chloride potassium (ACK) buffer for 5 minutes. For isolation of small intestinal IEL, Peyer's patches were first removed by dissection. Intestines were longitudinally cut and then cut into 1cm pieces and washed in PBS. Pieces were incubated in 30mL HBSS with 10% FBS, 10mM HEPES, and 1mM dithioerythritol with vigorous shaking at 37C for 30 minutes. Supernatants were collected, washed, and further isolated using a 40/67% discontinuous percoll density centrifugation for 20 minutes at room temp with no brakes.

Cell lines and *in vitro* cultures: B16-GP33 melanoma cell line were cultured in DMEM (Invitrogen) with 10% fetal bovine serum, 1% penicillin-streptomycin and 250 µg/ml G418 (Invitrogen #10131027). MCA-205 (Sigma) tumor line was maintained in RPMI supplemented with 10% FBS, 300 mg/L L-

glutamine, 100 units/mL penicillin, 100 μg/mL streptomycin, 1mM sodium pyruvate, 100μM NEAA, 1mM HEPES, 55μM 2-mercaptoethanol, and 0.2% Plasmocin mycoplasma prophylactic (InvivoGen). All the tumor cell lines were used for experiments when in the exponential growth phase. For *in vitro* T cell culture, splenocytes were activated in RPMI 1640 medium (Invitrogen) containing 10% fetal bovine serum and 1% penicillin-streptomycin, 2mM L-glutamine, 0.1 mg/ml GP33, beta-mercaptoethanol 50 mM and 10 U/ml IL-2.

Tumor engraftment and treatment of tumor-bearing mice (Fig. 5, 6): 3×10^5 B16-GP33 (Fig. 5), 5×10^5 B16-GP33 tumor cells (Fig. 6) were injected subcutaneously in 100 μl PBS. Around 0.5-1x10^6 $Cas9^+$ P14 T cells with CD45.1 markers were transferred to tumor on day 7 without pre-radiation of tumor-bearing mice. Tumors were measured every 2-3 days post-tumor engraftment for indicated treatments and calculated. Tumor volume was calculated by volume = (length × $width^2$)/2. For antibody-based treatment, tumor-bearing mice were treated with anti-PD1 antibody (200 μg per injection, clone RMP1-14, BioXcell) twice per week from day 7 post-tumor implantation. Tumor growth was measured twice per week with calipers. Survival events were recorded each time a mouse reached the endpoint (tumor volume ≥1,500 mm^3). Tumor weights were measured on day 23 for Fig. 5 and on day 25 for Fig. 6. All experiments were conducted according to the Salk Institute Animal Care and Use Committee.

Tumor digestion and cell isolation for Fig. 5: Tumors were minced into small pieces in RPMI containing 2% FBS, DNase I (0.5 μg/ml, Sigma-Aldrich), and collagenase (0.5 mg/ml, Sigma-Aldrich) and kept for digestion for 30 min at 37˚C, followed by filtration with 70 μm cell strainers (VWR). Filtered cells were incubated with ACK lysis buffer (Invitrogen) to lyse red blood cells, mixed with excessive RPMI 1640 medium (Invitrogen) containing 10% fetal bovine serum and 1% penicillin-streptomycin, and centrifuged at 400g for 5 min to obtain a single-cell suspension.

Proteasome activity analysis: For experiments involving the Proteasome Activity Probe (R&D systems), cells of interest were incubated with the probe at concentration of 2.5mM for 2 hours at 37C in PBS. Samples were washed and then stained with Zombie NIR viability dye (Biolegend) in PBS at 4C for 15 minutes. Samples were then stained with some variation of the following antibodies for 30 minutes in FACS Buffer on ice: CD45-BV510 (BD Biosciences), CD45.2-BV510 (Biolegend), CD45.1-PE-Cy7 (Invitrogen), CD4-APC Fire 810 (Biolegend), CD11b-Alexa Fluor 532 (Invitrogen), CD8-

Spark NIR 685 (Biolegend), CD44-Brilliant Violet 785 (Biolegend), CD62L-BV421 (BD Biosciences), PD1-BB700 (BD Biosciences), TIM-3-BV711 (Biolegend), LAG-3-APC-eFluor 780 (Invitrogen), SlamF6-APC (Invitrogen), CD39-Superbright 436 (Invitrogen), CX3CR1-PE/Fire 640 (Biolegend), CD69-PE-Cy5 (Biolegend), GITR-BV650 (BD Biosciences), CD27-BV750 (BD Biosciences). Samples were collected on a Cytek Northern Lights and analyzed via Cytek SpectraFlo software.

Tumor experiment for proteasome assay (Fig. 2): MCA-205 fibrosarcomas (2.5 x 10^5) were established via subcutaneous injection into the right flank of C57BL/6 mice. After 12-14 days of tumor growth, spleens, draining lymph nodes, and tumors from groups of mice were harvested and tumors were processed using the Mouse Tumor Dissociation Kit and gentleMACS dissociator (Miltenyi Biotec) according to manufacturer's protocol. For purification experiments, samples were pre-enriched using the EasySep Mouse $CD8^+$ T Cell Isolation Kit (Stemcell Technologies) according to manufacturer's protocol and stained with Live-or-Dye PE Fixable Viability Stain (Biotium) and CD8a-APC (Invitrogen) and live $CD8^+$ cells were sorted using the FACSAria II cell sorter. $CD8^+$ spleen and pooled TIL samples were washed in PBS and frozen for RNA-seq analysis. For adoptive cellular therapy experiments, B16-GP33 melanomas were established subcutaneously by injecting 5.0×10^5 cells into the right flank of CD45.1 mice and tumor-bearing hosts were irradiated with 5 Gy 24 hours prior to T cell transfer. In contrast, mice used in the experiments shown in Fig. 5 and Fig. 6 were not irradiated prior to T cell transfer. After 7 days of tumor growth, 1.5×10^6 CD45.2 OT-1 T cells and 1.5×10^6 CD45.1/CD45.2 P14 T cells were infused in 100 μL PBS via tail vein into tumor bearing mice. Tumors were harvested 14 days after adoptive cell transfer and CD8 TILs were analyzed for proteasome activity. All experiments were conducted in accordance with the guidelines of the University of North Carolina at Chapel Hill Animal Care and Use Committee.

Proteasome^{high}/Proteasome^{low} T cell adoptive transfer experiment (Fig. 2 and Extended Data Fig. 5c): For the adoptive transfer experiment involving proteasome^{high} and proteasome^{low} tumor-specific OT-1 T cells (Fig. 2l), whole splenocytes from OT-1 mice were activated with 1 μg/mL OVA_257–264 peptide and expanded for 7 days in the presence of 200 U/mL rhIL-2 (NCI). On day 7, OT-1 cells were FACS-sorted based on proteasome activity to isolate proteasome^{high} and proteasome^{low} OT-1 populations. A total of 2.5×10^5 sorted OT-1 cells were injected into C57BL/6 mice bearing B16F1-OVA melanomas. Tumors were established by subcutaneous injection of 3×10^5 B16F1-OVA cells into

the right flank 7 days prior to T cell transfer. Recipient mice were preconditioned with 5 Gy total body irradiation 24 hours before adoptive transfer. Tumor growth was measured every other day with calipers. For Extended Data Fig. 5c, MCA-205 fibrosarcomas (2.5 x 10^5) were established via subcutaneous injection into the right flank of C57BL/6 mice. After 14 days of tumor growth, Live $CD45^+$ $CD8^+$ $CD44^+$ $PD1^+$ T cells were sorted from tumors based on proteasome activity (high vs low) using the FACSAria II cell sorter. 2.5 x 10^4 cells were then injected into the 2 day MCA-205 bearing RAG2-/- hosts (n=5 per group) and tumor growth was monitored every other day starting on day 4. All experiments were conducted in accordance with the guidelines of the University of North Carolina at Chapel Hill Animal Care and Use Committee.

Retrovirus transduction and adoptive transfer: For overexpression of the gRNA retrovirus vector, 293T cells were transfected with the Eco-helper and MSCV gRNA vectors. 48 h and 72 h later, supernatant containing retroviral particles was ready for transduction. Donor P14 splenocytes were *in vitro* activated by 0.1 mg/ml GP33 and 10 U/ml IL-2 at 37°C for 24h, then spin-transduced (1500 g) with fresh RV supernatant from 293T cells for 90 min at 30°C in the presence of 5 μg/ml polybrene.

CRISPR-Cas9/RNP nucleofection: Naïve CD8+ T cells were enriched from spleen using the EasySep Mouse CD8+ T cell Isolation Kit (STEMCELL Technologies). sgRNAs targeting *ZSCAN20, JDP2, Etv5, Prdm1, Hic1* genes or the mouse or human genome nontargeting scramble (control) were obtained from Synthego, IDT, and GeneScript (Supplementary Table 5). Cas9 RNP was prepared immediately before experiments by incubating 1 μl sgRNA (stock: 3 nmol in 10 μl water), 0.6 μl Cas9 nuclease (IDT, stock: 62 μM) and 3.4 μl RNase-free water at room temperature for 10min. Nucleofection of naïve CD8+ T cells was performed using Lonza (Allendale, NJ) P3 primary cell kit and program DN100 with 4D-Nucleofector (Lonza Bioscience) for mouse and EO115 for human stimulated T cells . Each nucleofection reaction consisted of approximately 5-10 × 10^6 cells in 20 μl of nucleofection reagent and mixed with 5 μl of RNP: Cas9 complex. After electroporation, 100 μl of T cell culture media was added to the well to transfer the cells to 1.5 mL Eppendorf tube. The cells were rested at 37°C for 3 min. For *in vivo* adoptive transfer, cells were resuspended in PBS at desired concentration and adoptively transferred into recipient mice.

CRISPR gene editing validation via Sanger sequencing: The genomic DNA (gDNA) was isolated from both the KO-induced CD8+ T cells and the control cells using the Quick-DNA MicroPrep Kit (Zymo). The gDNA concentrations were quantified using the NanoDrop One spectrophotometer (ThermoFisher Scientific). Following isolation, PCR amplification was performed with 2x Phusion Plus Green PCR Master Mix (ThermoFisher Scientific) and the respective validation primers under the following conditions: (98 °C for 5 mins; 35 x of 98 °C for 10 secs, 69 °C for 20 secs, 72 °C for 20-30 secs/kb; 72 °C for 2 mins; hold at 10 °C). The PCR products were run on a 2% agarose gel with SYBR Safe DNA Gel Stain (Invitrogen), and the appropriate bands on the gel were extracted and purified with the Gel DNA Recovery Kit (Zymo). Concentrations of the purified amplicon samples were measured and then sent off for sequencing along with the designated sequencing primers designed from Benchling's Primer3 tool. The samples with the KOs were compared to the wildtype controls using EditCo's Ice Analysis software, providing the indel percentages, KO score, and the indel distributions used to assess the editing efficiency. Indel% ranges from 56% to 97%, and the KO score throughout experiments ranges from 32 to 74.

Flow cytometry, cell sorting, and antibodies: Both single cell suspensions were incubated with Fc receptor-blocking anti-CD16/32 (BioLegend) on ice for 10 min before staining. Cell suspensions were first stained with Red Dead Cell Stain Kit (ThermoFisher) for 10 min on ice. Surface proteins were then stained in FACS buffer (PBS containing 2% FBS and 0.1% sodium azide) for 30 min at 4˚C. To detect cytokine production *ex-vivo*, cell suspensions were re-suspended in RPMI 1640 containing 10% FBS, stimulated by 50 ng/ml PMA and 3 μM Ionomycin in the presence 2.5 μg/ml Brefeldin A (BioLegend #420601) for 4 h at 37°C. Cells were processed for surface marker staining as described above. For intracellular cytokine staining, cells were fixed in BD Cytofix/Cytoperm (BD #554714) for 30 min at 4 °C, then washed with 1× Permeabilization buffer (Invitrogen #00-8333-56). For transcription factor staining, cells were fixed in Foxp3 / Transcription Factor Fixation/Permeabilization buffer (Invitrogen #00-5521-00) for 30 min at 4 °C, then washed with 1× Permeabilization buffer. Cells were then stained with intraceulluar antibodies for 30 min at 4 °C. Samples were processed on LSR-II flow cytometer (BD Biosciences) and data were analyzed with FlowJo V10 (TreeStar). Cells were sorted either on FACSAria™ III sorter or Fusion sorter (BD Biosciences). The following antibodies against mouse proteins were used: anti-CD8a (53-6.7), anti-PD1 (29F.1A12), anti-CX3CR1 (SA011F11), anti-SLAMF6 (13G3), anti-CD38 (90), anti-CD39 (24DMS1), anti-CD101 (Moushi101), anti-KRLG1

(2F1), anti-CD69 (H1.2F3), anti-CD103 (M290), anti-CD62L (MEL-14), anti-Tim3 (RMT3-23), anti-Ly5.1 (A20), anti-Ly5.2 (104), anti-IFN-γ (XMG1.2), anti-TNF-α (MP6-XT22). The following antibodies against human proteins were used: anti-CD8a (RPA-T8), anti-CD4 (SK3), anti-CD45RA (H100), anti-CD45RO (UCHL1), anti-CCR7 (G043H7), anti-CD62L (DREG-56), anti-CD69 (FN50), anti-CD103 (Ber-ACT8), anti-CXCR6 (K041E5), anti-PD1 (EH12.2H7), anti-CD38 (HIT2), anti-CD39 (A1), anti-LAG3 (11C3C65), anti-Tim3 (F38-2E2), anti-TIGIT (A15153G), anti-IFN-γ (4S.B3), anti-TNF-α (MAb11), anti-IL 2 (JES6-5H4), anti-GZMB (QA16A02), anti-G4S Linker (E7O2V). These antibodies were purchased from Invitrogen, Biolegend, Cell Signaling, or eBiosciences.

***In vivo* individual TF KO phenotyping:** To assess the functional impact of individual TF KOs in $CD8^+$ T cells, we used Cas9-expressing P14 donor cells (LCMV-specific TCR transgenic mice, CD45.1 congenic) transduced with GFP-expressing retroviral vectors encoding individual gRNAs. Transductions were performed on the day of adoptive transfer without prior sorting. Without sorting, transduced donor cells (0.5-1 x 10^5) were immediately transferred into congenically distinct Cas9-expressing wild-type recipient mice (CD45.2) infected one day prior with either LCMV-Clone 13 or Armstrong strains. At ≥ day 20 post-infection, spleens from Clone 13 model and spleens and small intestines from Armstrong model were harvested. Single-cell suspensions were prepared and analyzed by flow cytometry. Live, single cells were first gated on $CD8^+$ cells, followed by gating on $CD45.1^+$ P14 donor $CD8^+$ T cells. Successfully transduced ($gRNA^+$) cells were identified by GFP expression, which ranged from 10% to 70% of P14 $CD8^+$ T cells across experiments. Due to variability in the number of GFP^+ donor P14 $CD8^+$ T cells obtained from different experiments, all phenotypic analyses were performed within the GFP^+ ($gRNA^+$) $CD45.1^+$ $CD8^+$ population. PD-1 positive and negative cells, exhaustion subsets (TEX_{term}: PD-1^+ $SLAMF6^-$ $CX3CR1^-$, TEX_{prog} :PD-1^+ $SLAMF6^+$ $CX3CR1^-$, TEX_{eff}: PD-1^+ $CX3CR1^+$) or expression of phenotypic markers was reported as a percentage within the $gRNA^+$ (GFP^+) P14 $CD8^+$ T cell population to ensure consistency across samples.

Co-transfers of control and TF KO/overexpression P14 $CD8^+$ T cells in infection or tumor models: Naive $CD8^+$ T cells were isolated from the spleens and lymph nodes of Cas9-expressing LCMV TCR transgenic (Cas9 P14) or P14 mice using the EasySep™ Mouse $CD8^+$ T Cell Isolation Kit (STEMCELL Technologies). Purified P14 cells were activated for ~24 hours on plates coated with goat anti-hamster

IgG (ThermoFisher), followed by 1 μg/mL hamster anti-mouse CD3 and 1 μg/mL hamster anti-mouse CD28 antibodies (ThermoFisher), in complete T cell medium (RPMI-1640 supplemented with 10% FBS (HyClone), 55 μM 2-mercaptoethanol, 100 IU/mL penicillin-streptomycin, and 1% HEPES). After activation, cells were transduced with retroviruses encoding Klf6 overexpression or gRNAs targeting Hic1 or Zscan20, and cultured with 20 IU/mL IL-2, 2.5 ng/mL IL-7, and 2.5 ng/mL IL-15 (PeproTech). At 48 hours post-transduction, reporter expression was confirmed by flow cytometry. Donor cell mixes were prepared using control vs. Klf6-overexpressing cells (Fig. 4), or gScramble vs. gHic1/gZscan20 cells (Fig. 5). For LCMV infection studies, 1.5×10^5 transduced P14 $CD8^+$ T cells were transferred into recipient mice, followed by infection with either 2×10^5 PFU LCMV-Armstrong (acute infection, intraperitoneal) or 2×10^6 PFU LCMV-Clone 13 (persistent infection, intravenous). For tumor studies, 5×10^5 to 1×10^6 transduced T cells (gScramble vs. gTF) were transferred on day 7 after B16-GP33 tumor implantation. All experiments were conducted according to the University of North Carolina at Chapel Hill Animal Care and Use Committee.

Perturb seq screening using the retroviral transcriptional factor library:

D*ual-guide direct-capture retroviral sgRNA vector.* To generate dual-guide sgRNA vector (MSCV-hU6-mU6-SV40-EGFP), we replaced the hU6 RNA scaffold region of the previously described retroviral sgRNA vector MG-guide[66] with an additional scaffold[67] and murine U6 promoter.

Dual-guide direct-capture retroviral library construction. For the curated gene list containing 21 TFs, a total of four gRNA sequences distributed on two individual constructs were designed for each gene. To construct the library, a customized double-strand DNA fragment pool containing 80 oligonucleotides targeting those 19 TFs and 4 scramble gRNAs (each oligonucleotide contains two guides targeting the same gene) (Supplementary Table 5) was ordered from IDT. The dual-guide library was generated using an In-Fusion (Takara) reaction. In brief, the gRNA containing DNA fragment pool was combined in MG-guide vector linearized with BpiI (Thermo Fisher). The construct was then transformed into Stellar competent cells (Takara) and amplified, and the resulting intermediate, individual construct was assessed for quality using Sanger sequencing. Then, individual dual-gRNA vectors were combined. For quality control, sgRNA skewing was measured using the MAGeCKFlute[68] to monitor how closely sgRNAs are represented in a library.

In vivo screening. Retrovirus was generated by co-transfecting HEK293 cells with the dual-guide, direct-capture retroviral TF library and the packaging plasmid pCL-Eco. Supernatants were collected at 48 and 72 hours post-transfection, then stored at −80 °C. Cas9-expressing P14 $CD8^+$ T cells were transduced with the viral supernatant to achieve a transduction efficiency of 20–30%. To ensure sufficient representation of control cells in downstream analysis, 50% of the viral mixture consisted of retrovirus encoding a non-targeting control gRNA vector. For in vivo experiments, 5×10^4 transduced P14 cells were intravenously transferred into Cas9-expressing, puromycin-resistant C57BL/6 recipient mice infected one day prior with either LCMV-Clone 13 or LCMV-Armstrong strain. A total of 25 LCMV-Clone 13 infected mice were used for five biological replicates, and 10 LCMV-Armstrong-infected mice were used for three biological replicates. Each biological replicate was labeled using hashtag antibodies (BioLegend, TotalSeq-C) to enable sample demultiplexing and statistical analysis. At ≥18 days post-infection, donor-derived P14 $CD8^+$ T cells were sorted and pooled for Perturb-seq analysis. Preliminary tests indicated that T cells expressing gRNA *in vivo* exhibit a greater tendency for gRNA silencing over extended periods compared to *ex vivo* cultured cells, despite initial successful KOs. To mitigate gRNA barcode silencing, we harvested tissue between days 18 and 23. Sorted $EGFP^+$ P14 $CD8^+$ T cells were resuspended and diluted in 10% FBS RPMI at a concentration of 1×10^6 cells per ml. Both the gene expression library and the CRISPR screening library were prepared using a Chromium Next GEM Single Cell 5′ kit with Feature Barcode technology for CRISPR Screening (10x Genomics). In brief, the single-cell suspensions were loaded onto the Chromium Controller according to their respective cell counts to generate 10,000 single-cell gel beads in emulsion per sample. Each sample was loaded into four separate channels. Chromium Next GEM Single Cell 5' Kit v2, PN-1000263, Chromium 5' Feature Barcode Kit, PN-1000541, 5' CRISPR Kit, PN-1000451, Chromium Next GEM Chip K Single Cell Kit, PN-1000287, Dual Index Kit TT Set A, PN-1000215, Dual Index Kit TN Set A, PN-1000250 (10x Genomics) in total were used for each reaction. The resulting libraries were quantified and quality checked using TapeStation (Agilent). Samples were diluted and loaded onto a NovaSeq (Illumina) using 100 cycle kit to obtain a minimum of 20,000 paired-end reads (26x91 bp) per cell for the gene expression library and 5,000 paired-end reads per cell for the CRISPR screening library, yielding an average of 42639, 36739, and 53413 reads aligned from cells from *in vivo* LCMV-Clone 13, *in vivo* LCMV-Armstrong infection, and *in vitro* donor respectively.

Data analysis. Alignments and count aggregation of gene expression and sgRNA reads were completed using Cell Ranger (v.7.0.1). Gene expression and sgRNA reads were aligned using the cell Ranger multi count command with default settings. Gene expression reads were aligned to the mouse genome (mm10 from ENSEMBL GRCm38 loaded from 10x Genomics). The median average of 4, 2, and 33 unique molecular identifiers (UMIs) were detected from cells from *in vivo* LCMV-Clone 13 and LCMV-Armstrong infection, and *in vitro* donor respectively. Droplets with sgRNA UMI passing of default Cell Ranger CRISPR analysis Protospacer UMI threshold were used in further analysis. The filtered feature matrices were imported into Seurat (v.4.3.0)[69] to create assays for a Seurat object containing both gene expression and CRISPR guide capture matrices. Cells detected with sgRNAs targeting two or more genes were then removed to avoid interference from multi-sgRNA-transduced cells. Low-quality cells with <200 detected genes, >10% mitochondrial reads, and <5% ribosomal reads were discarded. A total of 17,257 cells (Clone 13) and 15,211 cells (Armstrong) were passed quality filtering and were used for downstream analysis. Count data was normalized by a global-scaling normalization method and linear transformed.[70] Cluster-specific genes were identified using the FindAllMarkers function of Seurat. We utilized Nebulosa[71] to recover signals from sparse features in single-cell data and made gRNA density plots with scCustomize[72] based on kernel density estimation. In each biological replicate (Clone 13 n=5 and Armstrong =3), the percent cluster distribution of cells with each TF gRNA vector was calculated. Among two gRNA vectors per target TF, the gRNA vector with higher TEX_{term} reduction was shown in Fig. 3d and utilized for Perturb-seq in LCMV-Armstrong infection (Supplementary Table 5). Two-way ANOVA with Fisher's LSD test was performed to determine statistical significance. DEG was calculated using the MAST model[73], the results were then used as inputs for GSEA to evaluate the effect on selected pathways. Genes with p-value < 0.05 were considered as DEG.

UMAP plots were generated by calculating UMAP embeddings using Seurat and then plotting them as scatter plots using ggplot2. Kernel density calculations for each gRNA were performed on UMAP embeddings using the MASS package via the kde2d function. The kernel density results were plotted as a raster layer with ggplot2 over the UMAP scatter plots. Finally, density contour lines were added using ggplot2's built-in 2D kernel density contour geom (geom_density_2d).

ATAC-Seq library preparation and sequencing: ATAC-seq was performed as previously described[74]. Briefly, 5,000-50,000 viable cells were washed with cold PBS, collected by centrifugation, then lysed in resuspension buffer (RSB) (10 mM Tris-HCl, pH 7.4, 10 mM NaCl, 3 mM MgCl2)

supplemented with 0.1% NP40, 0.1% Tween-20, and 0.01% digitonin. Samples were incubated on ice for 3 min, then washed out with 1 ml RSB containing 0.1% Tween-20. Nuclei were pelleted by centrifugation at 500g for 10 min at 4°C then resuspended in 50 ul transposition mix (25ul 2x TD buffer, 2.5 ul transposase (100 nM final), 16.5 ul PBS, 0.5 ul 1% digitonin, 0.5 ul 10% Tween-20, 5 ul H2O) and incubated at 37°C for 30 min in a thermomixer with 1000 RPM mixing. DNA was purified using a Qiagen MinElute PCR cleanup kit, then PCR amplified using indexed oligos. The optimal number of amplification cycles for each sample was determined by qPCR. Libraries were size selected using AmpureXP beads and sequenced using an Illumina NextSeq500 for 75bp paired-end reads.

ATAC-Seq analysis: Paired-end 42-bp, or paired-end 75-bp reads were aligned to the M. musculus mm10 genome using BWA[75,76]with parameters "bwa mem -M -k 32". ATAC-seq peaks were called using MACS2[77] program using parameters "callpeaks -qvalue 5.0e-2 –shift -100 –extsize 200". Differentially accessible regions were identified using DESeq2[78] . Batch effect was removed using limma[79]. Heatmap visualization of ATAC-seq data was performed using pheatmap.

Single-cell RNA sequencing metadata analysis: Analysis was primarily performed in R (v 3.6.1) using the package Seurat (v 3.1)[69,80], with the package tidyverse (v 1.2.1)[81] used to organize data and the package ggplot2 (v 3.2.1) used to generate figures. scRNA-seq data from GSE10898, GSE99254, GSE98638, GSE199565, and GSE181785 were filtered to keep cells with a low percentage of mitochondrial genes in the transcriptome (< 5%) and between 200 and 3000 unique genes to exclude poor quality reads and doublets. Cell cycle scores were regressed when scaling gene expression values and T cell receptor genes were regressed during the clustering process, which was performed with the Louvain algorithm within Seurat and visualized with UMAP. To quantify the gene expression patterns, we used Seurat's module score feature to score each cluster based on its per cell expression of TFs.

To obtain Extended Data Fig. 5a, raw single-cell count data and cell annotation data was downloaded from NCBI GEO (GSE99254)[45]. Count data was normalized and transformed by derivation of the residuals from a regularized negative binomial regression model for each gene (SCT normalization method in Seurat[87], v4.1.1), with 5000 variable features retained for downstream dimensionality reduction techniques. Integration of data was performed on the patient level with Canonical Correlation Analysis as the dimension reduction technique[82]. Principal component analysis and UMAP dimension

reduction were performed, with the first 50 PCs utilized in UMAP generation. Cells were clustered utilizing the Louvain algorithm with multi-level refinement. The data was subset to CD8+ T cells, which were identified utilizing the labels provided by Guo et al[66]. Cell type labels were confirmed via 1) SingleR[83] (v1.8.1) annotation utilizing the ImmGen[84] database obtained via celda(1.10), 2) cluster marker identification, and 3) cell type annotation with the ProjecTILs T cell atlas[7] (v2.2.1). After sub-setting to $CD8^+$ T cells, cells were again normalized utilizing SCT normalization, with 3000 variable features retained for dimension reduction. Due to the low number of cells on the per-patient level, HArmstrongony[85](v1.0) was utilized to integrate the data at the patient level, rather than Seurat. PCA and UMAP dimensionality reduction were performed as above.

Statistical analyses: Statistical tests for flow cytometry data were performed using Graphpad Prism 10. *p-values* were calculated using either two-tailed unpaired Student's t-tests, one-way ANOVA or two-way ANOVA as indicated in each figure. Linear regressions were performed using the ordinary least squares method in R (v 3.6.1). All data were presented as the mean ± s.e.m. The *P* values were represented as follows: ****$P < 0.0001$, ***$P < 0.001$, **$P < 0.01$, and *$P < 0.05$.

Data availability

ATAC-sequencing data from this paper will be deposited in the GEO database (GSE279498). Taiji v2.0 output of this study (TF activity atlas, TF-TF interaction maps, and TF activity on genome browser view) will be available at our $CD8^+$ T cell TF atlas portal (https://wangweilab.shinyapps.io/Tcellstates/) and interactive interface for TF atlas exploration (https://huggingface.co/spaces/taijichat/chat).
All other raw data are available from the corresponding author upon request.

Code availability

All scripts and the Taiji v2.0 package are uploaded to GitHub (https://github.com/Wang-lab-UCSD/Taiji2).

Methods references

61. Zheng, C. *et al.* Landscape of Infiltrating T Cells in Liver Cancer Revealed by Single-Cell Sequencing. *Cell* **169**, 1342–1356.e16 (2017).
62. Weirauch, M. T. *et al.* Determination and Inference of Eukaryotic Transcription Factor Sequence Specificity. *Cell* vol. 158 1431–1443 Preprint at https://doi.org/10.1016/j.cell.2014.08.009 (2014).
63. Zhao, T., Liu, H., Roeder, K., Lafferty, J. & Wasserman, L. The huge Package for High-dimensional Undirected Graph Estimation in R. (2020) doi:10.48550/arXiv.2006.14781.
64. Traag, V. A., Waltman, L. & van Eck, N. J. From Louvain to Leiden: guaranteeing well-connected communities. *Sci. Rep.* **9**, 5233 (2019).
65. Schönfeld, M. & Pfeffer, J. Fruchterman/Reingold (1991): Graph Drawing by Force-Directed Placement. *Schlüsselwerke der Netzwerkforschung* 217–220 Preprint at https://doi.org/10.1007/978-3-658-21742-6_49 (2019).
66. Bailis, W. *et al.* Author Correction: Distinct modes of mitochondrial metabolism uncouple T cell differentiation and function. *Nature* **573**, E2 (2019).
67. Cong, L. *et al.* Multiplex genome engineering using CRISPR/Cas systems. *Science* **339**, 819–823 (2013).
68. Wang, B. *et al.* Integrative analysis of pooled CRISPR genetic screens using MAGeCKFlute. *Nat. Protoc.* **14**, 756–780 (2019).
69. Stuart, T. *et al.* Comprehensive Integration of Single-Cell Data. *Cell* vol. 177 1888–1902.e21 Preprint at https://doi.org/10.1016/j.cell.2019.05.031 (2019).
70. Hafemeister, C. & Satija, R. Normalization and variance stabilization of single-cell RNA-seq data using regularized negative binomial regression. *Genome Biol.* **20**, 296 (2019).
71. Alquicira-Hernandez, J. & Powell, J. E. Nebulosa recovers single-cell gene expression signals by kernel density estimation. *Bioinformatics* **37**, 2485–2487 (2021).
72. Marsh, S. E. scCustomize: custom visualizations & functions for streamlined analyses of single cell sequencing. *Preprint at https://doi. org/10.5281/zenodo*.
73. Finak, G. *et al.* MAST: a flexible statistical framework for assessing transcriptional changes and characterizing heterogeneity in single-cell RNA sequencing data. *Genome Biol.* **16**, 278 (2015).
74. McDonald, B. *et al.* Canonical BAF complex activity shapes the enhancer landscape that licenses CD8 T cell effector and memory fates. *Immunity* **56**, 1303–1319.e5 (2023).
75. Li, H. & Durbin, R. Fast and accurate short read alignment with Burrows-Wheeler transform.

Bioinformatics **25**, (2009).
76. Li, H. & Durbin, R. Fast and accurate long-read alignment with Burrows-Wheeler transform. *Bioinformatics* **26**, (2010).
77. Zhang, Y. *et al.* Model-based Analysis of ChIP-Seq (MACS). *Genome Biol.* **9**, 1–9 (2008).
78. Love, M. I., Huber, W. & Anders, S. Moderated estimation of fold change and dispersion for RNA-seq data with DESeq2. *Genome Biol.* **15**, 1–21 (2014).
79. Ritchie, M. E. *et al.* limma powers differential expression analyses for RNA-sequencing and microarray studies. *Nucleic Acids Res.* **43**, e47 (2015).
80. Butler, A., Hoffman, P., Smibert, P., Papalexi, E. & Satija, R. Integrating single-cell transcriptomic data across different conditions, technologies, and species. *Nat. Biotechnol.* **36**, 411–420 (2018).
81. Wickham, H. *et al.* Welcome to the Tidyverse. *Journal of Open Source Software* vol. 4 1686 Preprint at https://doi.org/10.21105/joss.01686 (2019).
82. Hao, Y. *et al.* Integrated analysis of multimodal single-cell data. *Cell* **184**, 3573–3587.e29 (2021).
83. Aran, D. *et al.* Reference-based analysis of lung single-cell sequencing reveals a transitional profibrotic macrophage. *Nat. Immunol.* **20**, 163–172 (2019).
84. Heng, T. S. P., Painter, M. W. & Immunological Genome Project Consortium. The Immunological Genome Project: networks of gene expression in immune cells. *Nat. Immunol.* **9**, 1091–1094 (2008).
85. Korsunsky, I. *et al.* Fast, sensitive and accurate integration of single-cell data with Harmony. *Nat. Methods* **16**, 1289–1296 (2019).
86. Zhang, L. *et al.* Single-Cell Analyses Inform Mechanisms of Myeloid-Targeted Therapies in Colon Cancer. *Cell* **181**, 442–459.e29 (2020).

Acknowledgments

We thank members of the Chung, Kaech, and Wang laboratory for their advice and assistance with experiments. We appreciate UNC Lineberger Preclinical Research Unit at the University of North Carolina at Chapel Hill assisted animal experiments which is supported in part by an NCI Center Core Support Grant (CA16086) to the UNC Lineberger Comprehensive Cancer Center. This work was supported by NIH grants to S.M.K. R37AI066232, R01AI123864, R21AI151986, and R01CA240909, to W.W. R01AI150282, R01HG009626 (in part) to H.K.C. K01EB034321, to J.J.M. R01AI177864 to J.E.T. R01CA248359 and R01CA244361, to D.C.H. AI151123, to Y.W. EB029122 and GM140929, and to L.L. K01EB035649. H.K.C. is a Damon Runyon Fellow supported by Damon Runyon Cancer Research Foundation grant [DRG-2374-19].

Author contributions

H.K.C. designed and performed experiments. A.B., B.M.R., F.X., Y.L., K.Y., D.J., M.S., J.G., S.M., E.C., B.M. D.C., B.C., Q.Y., F.H., T.H.M., S.K.V., V.T., U.H.C., G.D., B.S., Y.W., L.L., P.H., and J.H. assist with experiments. H.K.C., C.L., A.J., N.J.B., M.S. analyzed the sequencing and bioinformatics data. J.W., B.M., M.S., Y.H., L.H., U.H.C., J.M., contribute to bioinformatics data analysis. Z.W., A.W. contributed to TaijiChat and portal generation. J.H. and D.H. provided resources and training for ATAC-sequencing. B.P.R. and J.E.T. performed proteasome activity experiments. H.K.C., S.M.K., W.W., Y.W., L.L., B.S., G.P., J.E.T., J.J.M., D.C.H, provided scientific input and acquired funding. H.K.C, and C.L. wrote the original manuscript. H.K.C., W.W., and S.M.K. reviewed and edited the paper. H.K.C., S.M.K., and W.W. conceptualized, designed, and supervised the study.

Competing interests

S.M.K. is SAB member for Pfizer, EvolveImmune Therapeutics, Arvinas and Affini-T, advisor for Barer Institute of Raphael Holdings and Academic Editor at Journal of Experimental Medicine. The remaining authors declare no conflict of interest.

Additional information

Supplementary Information is available for this paper. Correspondence and requests for materials should be addressed to H. Kay Chung (hkchung@unc.edu), Susan M. Kaech (skaech@salk.edu), and Wei Wang (wei-wang@ucsd.edu).

Extended Data Figure Legends

Extended Data Fig. 1 | Parallel differentiation of T_{RM} and TEX_{term} and their transactional and epigenetic similarity. a, UMAP of scRNA-seq data of T cells from blood, tumor, and adjacent normal tissues of CRC[86], NSCLC[45], and HCC[61] patients. Unbiased clustering identified multiple T cell states consistent with those observed murine LCMV infection and tumors. **b,** T_{RM} marker genes show higher expression in TEX_{term} cluster from Pan-cancer scRNA-seq in **a**. **c,** Both T_{RM} and TEX_{term} clusters upregulate exhaustion-[8] and T_{RM}[35]-associated gene signatures. **d,** Pearson correlation matrix of batch-corrected ATAC-seq datasets[3,9,33,34]. Color and size are both proportional to correlation strength. **e,** A total of 121 experiments across multiple data sets[3,9,18,23,32–36] were utilized to generate an epigenetic and transcriptional atlas of $CD8^+$ T cells under chronic and acute antigen exposure.

Extended Data Fig. 2 | Cataloging key TFs across $CD8^+$ T cell states. a, Logic flow of the unbiased PageRank comparison to classify single-state/multi-state TFs. **b,** Number of TFs catalogued in each cell state. **c,** Venn Diagrams showing overlap of TFs with the T_{RM} cell state. **d,** TF activity score (normalized PageRank) of previously reported TEX_{term}-preventing TFs (TFAP4, JUN, BATF3, and BATF), newly identified TEX_{term} single-state TFs (JDP2, ZFP324, ZBTB49, ZFP143, ZSCAN20), and NFATC1, a known TEX_{term}-associated TF.

Extended Data Fig. 3 | TF wave analysis. a, Schematic of the analysis pipeline. **b,** Selection of algorithms and parameters for TF wave analysis. The Pearson correlation was chosen for the distance metric, with k=7 chosen as the optimal cluster number. **c,** Seven TF waves. Circles represent specific cell states. Red color indicates normalized PageRank scores. **d,** List of TF members in each wave. **e**, Heatmap of biological pathways enriched in each TF wave. Red-blue color scale indicates the p-value.

Extended Data Fig. 4 | TF–TF association network in TEX_{term} and T_{RM} cell states. a–c, TF–TF associations of (**a**) TEX_{term} single-state TFs (JDP2, ZFP324, and IRF8); (**b**) T_{RM} single-state TFs (FOSB, SNAI1, and KLF6); (**c**) multi-state TFs shared by TEX_{term} and T_{RM} (PRDM1, FLI1, and GFI1); and (**d**) previously reported TFs whose OE prevent TEXterm–JUN, TFAP4, and BATF. Line color indicates state specificity: T_{RM} (green) or TEX_{term} (brown) state. Line thickness represents interaction intensity. Line color indicates state specificity: T_{RM} (green) or TEX_{term} (brown) state. Line thickness represents interaction intensity.

Extended Data Fig. 5 | TF network analysis reveals proteasome pathway enrichment in TEX_{term} state with diminished tumor control function. a, Pseudotime analysis of $CD8^+$ TIL scRNA-seq data from NSCLC patients (n = 14), showing a positive correlation between proteasome gene scores (KEGG: M10680) and T cell exhaustion. **b,** Gene set enrichment analysis (GO:0043161, Proteasome-mediated ubiquitin-dependent protein catabolic process) of RNA-seq from $CD8^+$ splenocytes (black) and TILs (purple), n = 3 each. **c,** Tumor growth of $Rag2^{-/-}$ mice bearing MCA-205 sarcomas infused with $proteasome^{high}$ or $proteasome^{low}$ $CD8^+$ TILs isolated from C57BL/6 mice bearing MCA-205 tumors. n = 5 per group. Two-way ANOVA Tukey's multiple comparison test were performed. ****P<0.0001, ***P<0.001, **P<0.01, *P<0.05.

Extended Data Fig. 6 | *in vivo* Perturb-seq with dual-guide RNA in LCMV chronic infection and individual validation. a, Retroviral vector design for dual-gRNA delivery. **b,** Feature plot of differentiation markers (Pan-exhaustion: red, TEX_{prog}: pink, TEX_{eff}: blue, Cell cycle: purple, TEX_{term}: brown). **c,** Heatmap of marker gene expression across cell state clusters identified by Seurat's Find Markers() function. **d,** Frequency of $PD1^+$ $SLAMF6^-$ $CD101^+$ cells (**d**). Frequency of $CD38^+$ $CD39^+$ double-positive cells (**e**). Statistical analysis: Ordinary one-way ANOVA with Dunnett's multiple comparisons test versus gScramble (n ≥ 5 from ≥2 biological replicates). Data are presented as mean ± s.e.m. ****P< 0.0001; ***P < 0.001; **P < 0.01; *P < 0.05.

Extended Data Fig. 7 | Single-cell transcriptomic profiling of $CD8^+$ T cells from Perturb-seq in acute LCMV infection and validation of the selectivity of T_{RM} single-state TF, *Klf6* overexpression. a, Feature plots of differentiation marker genes (T_{CM}: yellow, T_{EM}: blue, T_{RM}-*Itgae*^{low}: dark blue, T_{RM}: green). **b,** Heatmap of differentially expressed genes between T_{RM}-*Itgae*^{low} and T_{RM} clusters. **c,** Volcano plots of differentially expressed genes in $Cas9^+$ P14 $CD8^+$ T cells expressing *gEtv5*, *gArid3a*, g*Hic1*, or *gGfi1*. **d,** T_{RM} single-state TF, *Klf6* overexpression does not accelerate T cell exhaustion. Experimental setup: *Klf6*-RV or control-RV transduced P14 $CD8^+$ T cells co-transferred into mice infected with chronic LCMV-Clone 13**,** Quantification of the frequency of $PD1^+$, TEX_{prog} ($PD1^+$ $SLAMF6^+$ $CX3CR1^-$), TEX_{eff} ($PD1^+$ $SLAMF6^-$ $CX3CR1^+$) and TEX_{term} ($PD1^+$ $SLAMF6^-$ $CX3CR1^-$) populations. Paired t-tests (n ≥ 6 from ≥2 biological replicates). Data are presented as mean ± s.e.m. ****P <0.0001, ***P < 0.001, **P < 0.01, *P < 0.05.

Extended Data Fig. 8 | Depletion of TEX_{term}-single state TF, *Zscan20* and TEX_{term} and T_{RM} multi-state TF, *Hic1* reduces T cell exhaustion. a, Co-transfer of $Cas9^+$ P14 $CD8^+$ T cells transduced with RV-g*Zscan20* or RV-g*Hic1*, mixed with gRNA control RV transduced cells into B16-GP33 tumor-bearing mice. **b,** Representative flow plots of $PD1^+$ P14 $CD8^+$ T cells stained for SLAMF6 and CX3CR1. **c-e,** Quantification of (**c**) TEX_{prog} ($PD1^+$ $SLAMF6^+$ $TIM3^-$), (**d**) TEX_{term} ($PD1^+$ $SLAMF6^-$ $CX3CR1^-$), and (**e**) non-progenitor, exhausted ($PD1^+$ $SLAMF6^-$ $TIM3^+$) popultation. Paired t-tests ($n \geq 6$ from ≥ 2 biological replicates). Data are presented as mean ± s.e.m. ****$P < 0.0001$, ***$P < 0.001$, **$P < 0.01$, *$P < 0.05$.

Extended Data Fig. 9 | Conservation of single- and multi-state TFs in human pan-cancer TEX_{term} and T_{RM} cell states. a, Human pan-cancer datasets utilized in this study[49–56]. **b,** Cluster-specific marker mRNA expression across integrated pan-cancer single-cell multi-omics datasets. **c,** TF activity analysis using Taiji on matched matched scRNA-seq and scATAC-seq datasets from various human cancers, including ccRCC, GBM, BCC, HNSCC, HCC, and RCC. $CD8^+$ T cell states were annotated using canonical marker gene expression. PageRank scores derived from Taiji were log-transformed, averaged per state, and z-score normalized. Results were visualized with a focus on TF activity T_{RM} and TEX_{term} cell states. **d,** mRNA expression of TFs were compared across human $CD8^+$ T cell states. The dataset encompassed T cells from 15 tumor types. Cell type annotations provided by the original study were retained and mapped to the following broad categories of clusters: T_{RM}, TEX_{term}, T_{EM}, Memory, Naive, and cell cycle. Seurat's AverageExpression function was used, followed by z-score normalization. Data visualization emphasized comparisons between T_{RM} and TEX_{term} cell states. Cell-state-selectivity conserved TFs in humans and mice are highlighted in bold (**c, d**).

Extended Data Fig. 10 | CRISPR validation of TEX_{term} single-state TF KO in human PBMCs and antitumor activity of TF-deficient T cells in mice. Indel frequencies, representative Sanger sequencing traces, and indel distributions for (**a**) *ZSCAN20* and (**b**) *JDP2* KOs. **c,** Survival of B16-GP33 bearing mice receiving *Zscan20* KO or control P14 $CD8^+$ T cells, followed by anti-PD1 or isotype IgG2a treatment. **d,** Survival of tumor-bearing mice with *Jdp2* KO P14 $CD8^+$ T cell transfer.

Supplementary Tables

Supplementary Table 1 | Composition of multi-omic atlas

Supplementary Table 2 | TF PageRank scores of multi-state and single-state TFs

Supplementary Table 3 | TF PageRank scores of T_{RM}- and TEX_{term} single-state TFs and multi-state TFs

Supplementary Table 4 | Catalog of cell-state important TFs

Supplementary Table 5 | Catalog of TF communities in T_{RM} and TEX_{term}

Supplementary Table 6 | gRNA sequences for TF gRNA library and RNP gRNA

Supplementary Table 7 | Perturb seq cluster statistics (Fig. 3 and Fig. 4)

Supplementary Table 8 | Gene signatures

Supplementary Methods

TaijiChat: An Integrated Conversational Interface for Multi-Omics Data Exploration**.**

Figure 1

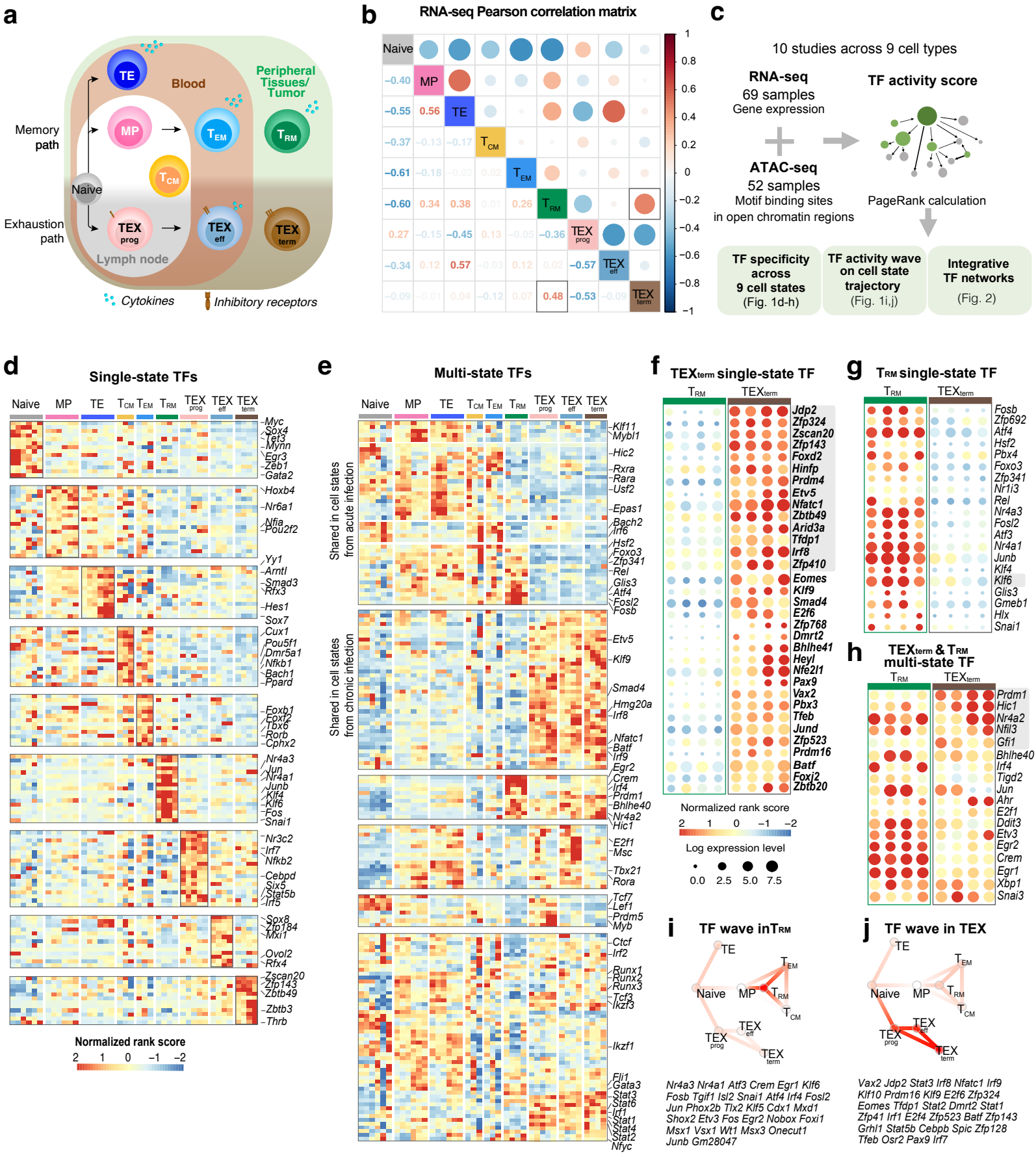
a
Blood
Peripheral Tissues/ Tumor
Memory path
Exhaustion path
Naive
MP
TE
TEM
TRM
TCM
TEX prog
TEX eff
TEX term
Lymph node
Cytokines
Inhibitory receptors
b
RNA-seq Pearson correlation matrix
c
10 studies across 9 cell types
RNA-seq
69 samples
Gene expression
ATAC-seq
52 samples
Motif binding sites in open chromatin regions
TF activity score
PageRank calculation
TF specificity across 9 cell states (Fig. 1d-h)
TF activity wave on cell state trajectory (Fig. 1i,j)
Integrative TF networks (Fig. 2)
d
Single-state TFs
Normalized rank score
e
Multi-state TFs
Shared in cell states from acute infection
Shared in cell states from chronic infection
f
TEXterm single-state TF
Normalized rank score
Log expression level
g
TRM single-state TF
h
TEXterm & TRM multi-state TF
i
TF wave inTRM
Nr4a3 Nr4a1 Atf3 Crem Egr1 Klf6 Fosb Tgif1 Isl2 Snai1 Atf4 Irf4 Fosl2 Jun Phox2b Tlx2 Klf5 Cdx1 Mxd1 Shox2 Etv3 Fos Egr2 Nobox Foxi1 Msx1 Vsx1 Wt1 Msx3 Onecut1 Junb Gm28047
j
TF wave in TEX
Vax2 Jdp2 Stat3 Irf8 Nfatc1 Irf9 Klf10 Prdm16 Klf9 E2f6 Zfp324 Eomes Tfdp1 Stat2 Dmrt2 Stat1 Zfp41 Irf1 E2f4 Zfp523 Batf Zfp143 Grhl1 Stat5b Cebpb Spic Zfp128 Tfeb Osr2 Pax9 Irf7

Figure 2

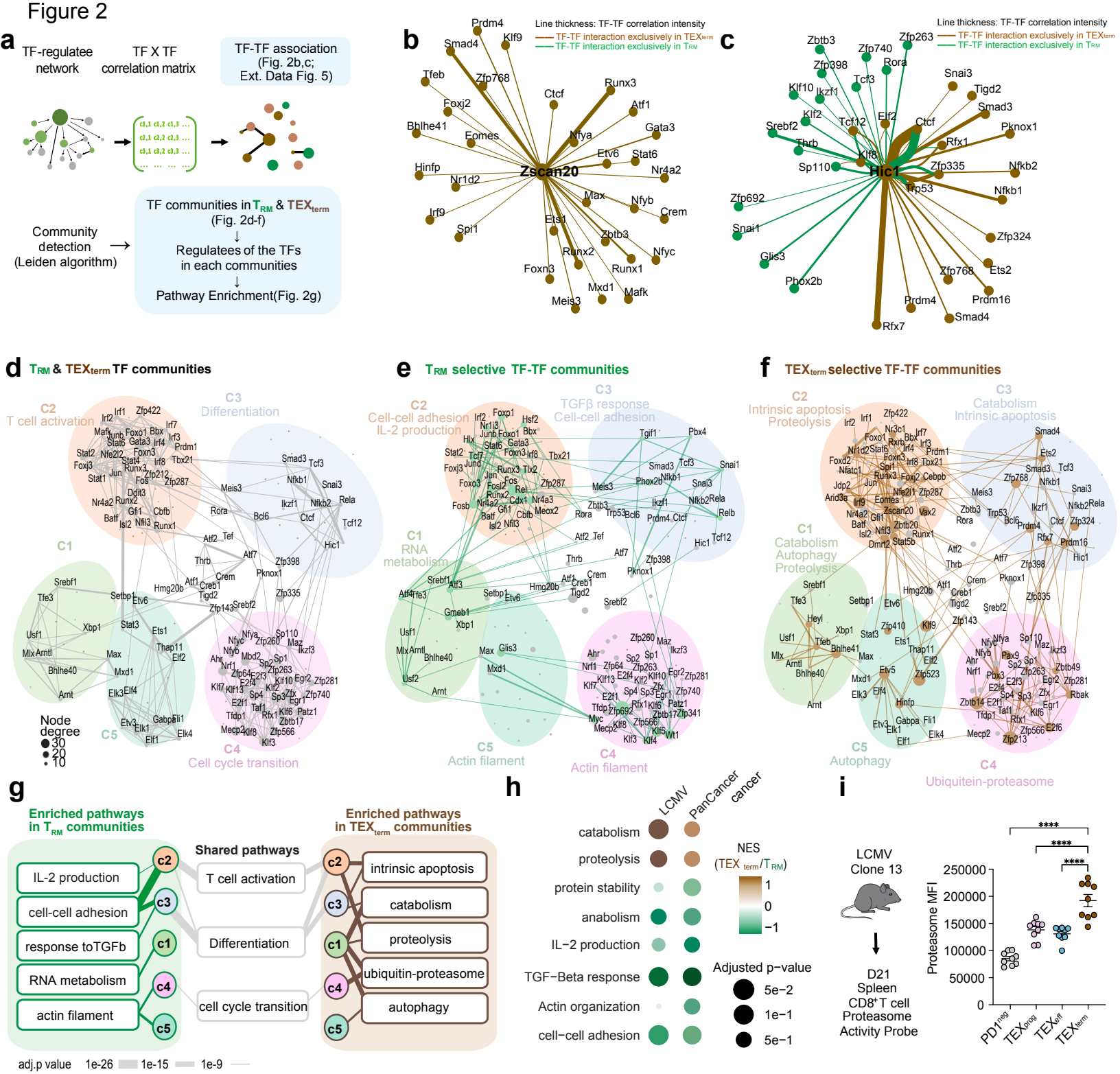
a
TF-regulatee network
TF X TF correlation matrix
TF-TF association (Fig. 2b,c; Ext. Data Fig. 5)
Community detection (Leiden algorithm)
TF communities in T_RM & TEX_term (Fig. 2d-f)
Regulatees of the TFs in each communities
Pathway Enrichment(Fig. 2g)
b
Line thickness: TF-TF correlation intensity
TF-TF interaction exclusively in TEXterm
TF-TF interaction exclusively in TRM
Zscan20
c
Hic1
d
TRM & TEXterm TF communities
C1
C2 T cell activation
C3 Differentiation
C4 Cell cycle transition
C5
Node degree
e
TRM selective TF-TF communities
C1 RNA metabolism
C2 Cell-cell adhesion IL-2 production
C3 TGFβ response Cell-cell adhesion
C4 Actin filament
C5 Actin filament
f
TEXterm selective TF-TF communities
C1 Catabolism Autophagy Proteolysis
C2 Intrinsic apoptosis Proteolysis
C3 Catabolism Intrinsic apoptosis
C4 Ubiquitein-proteasome
C5 Autophagy
g
Enriched pathways in T_RM communities
IL-2 production
cell-cell adhesion
response toTGFb
RNA metabolism
actin filament
Shared pathways
T cell activation
Differentiation
cell cycle transition
Enriched pathways in TEX_term communities
intrinsic apoptosis
catabolism
proteolysis
ubiquitin-proteasome
autophagy
adj.p value 1e-26 1e-15 1e-9
h
LCMV
PanCancer
cancer
catabolism
proteolysis
protein stability
anabolism
IL−2 production
TGF−Beta response
Actin organization
cell−cell adhesion
NES (TEX term/T RM)
Adjusted p−value
5e−2
1e−1
5e−1
i
LCMV Clone 13
D21 Spleen CD8+ T cell Proteasome Activity Probe
Proteasome MFI
PD1neg
TEXprog
TEXeff
TEXterm
j
MCA sarcomas
D14 CD8+TILs Proteasome activity
Proteasome activity (MFI)
PD1- Tim3-
PD1+ Tim3-
PD1+ Tim3+
k
B16-GP33 melanoma
D7 transfer OT-1 & P14
D14 CD8+TILs Proteasome activity
Proteasome activity (MFI)
Endogenous
OT-1
P14
l
OVA antigen-specific OT1 T cells
B16F1-OVA
D7
Proteasome activity sort & transfer
B16F1-OVA tumor mice
High
Low
Tumor growth
No T Cells
Proteasome low
Proteasome high
Tumor Size (mm3)
Days post-implantation

Figure 3

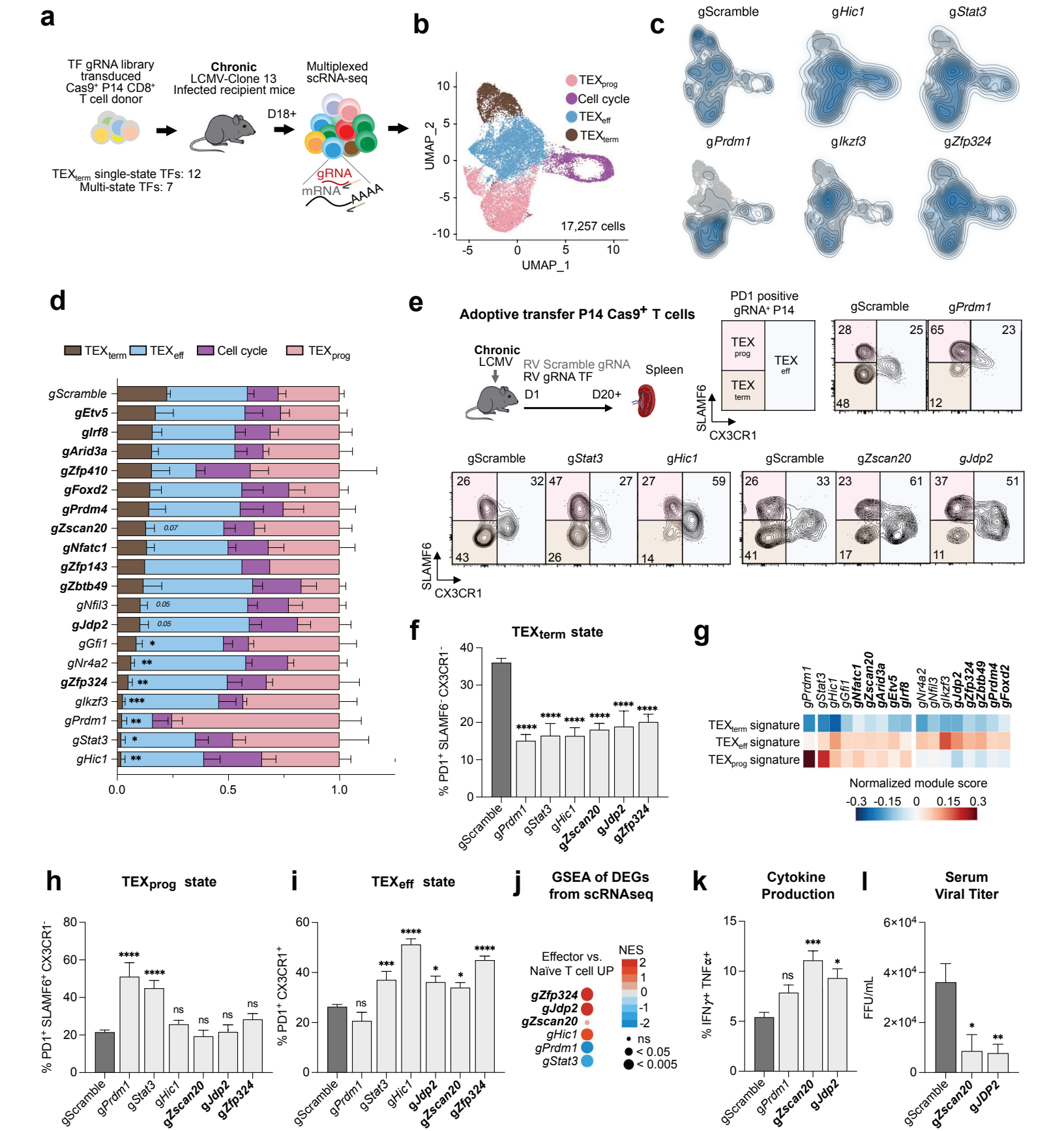
a
TF gRNA library transduced Cas9+ P14 CD8+ T cell donor
Chronic LCMV-Clone 13 Infected recipient mice
D18+
Multiplexed scRNA-seq
gRNA
mRNA
AAAA
TEXterm single-state TFs: 12
Multi-state TFs: 7
b
TEXprog
Cell cycle
TEXeff
TEXterm
17,257 cells
UMAP_2
UMAP_1
c
gScramble
gHic1
gStat3
gPrdm1
gIkzf3
gZfp324
d
TEXterm
TEXeff
Cell cycle
TEXprog
gScramble
gEtv5
gIrf8
gArid3a
gZfp410
gFoxd2
gPrdm4
gZscan20
gNfatc1
gZfp143
gZbtb49
gNfil3
gJdp2
gGfi1
gNr4a2
gZfp324
gIkzf3
gPrdm1
gStat3
gHic1
e
Adoptive transfer P14 Cas9+ T cells
Chronic LCMV
RV Scramble gRNA
RV gRNA TF
D1
D20+
Spleen
PD1 positive gRNA+ P14
TEX prog
TEX term
TEX eff
SLAMF6
CX3CR1
gScramble
gPrdm1
gStat3
gHic1
gZscan20
gJdp2
f
TEXterm state
% PD1+ SLAMF6- CX3CR1-
gScramble
gPrdm1
gStat3
gHic1
gZscan20
gJdp2
gZfp324
g
TEXterm signature
TEXeff signature
TEXprog signature
Normalized module score
h
TEXprog state
% PD1+ SLAMF6+ CX3CR1-
i
TEXeff state
% PD1+ CX3CR1+
j
GSEA of DEGs from scRNAseq
Effector vs. Naïve T cell UP
NES
gZfp324
gJdp2
gZscan20
gHic1
gPrdm1
gStat3
ns
< 0.05
< 0.005
k
Cytokine Production
% IFNγ+ TNFα+
l
Serum Viral Titer
FFU/mL
gJDP2

Figure 4

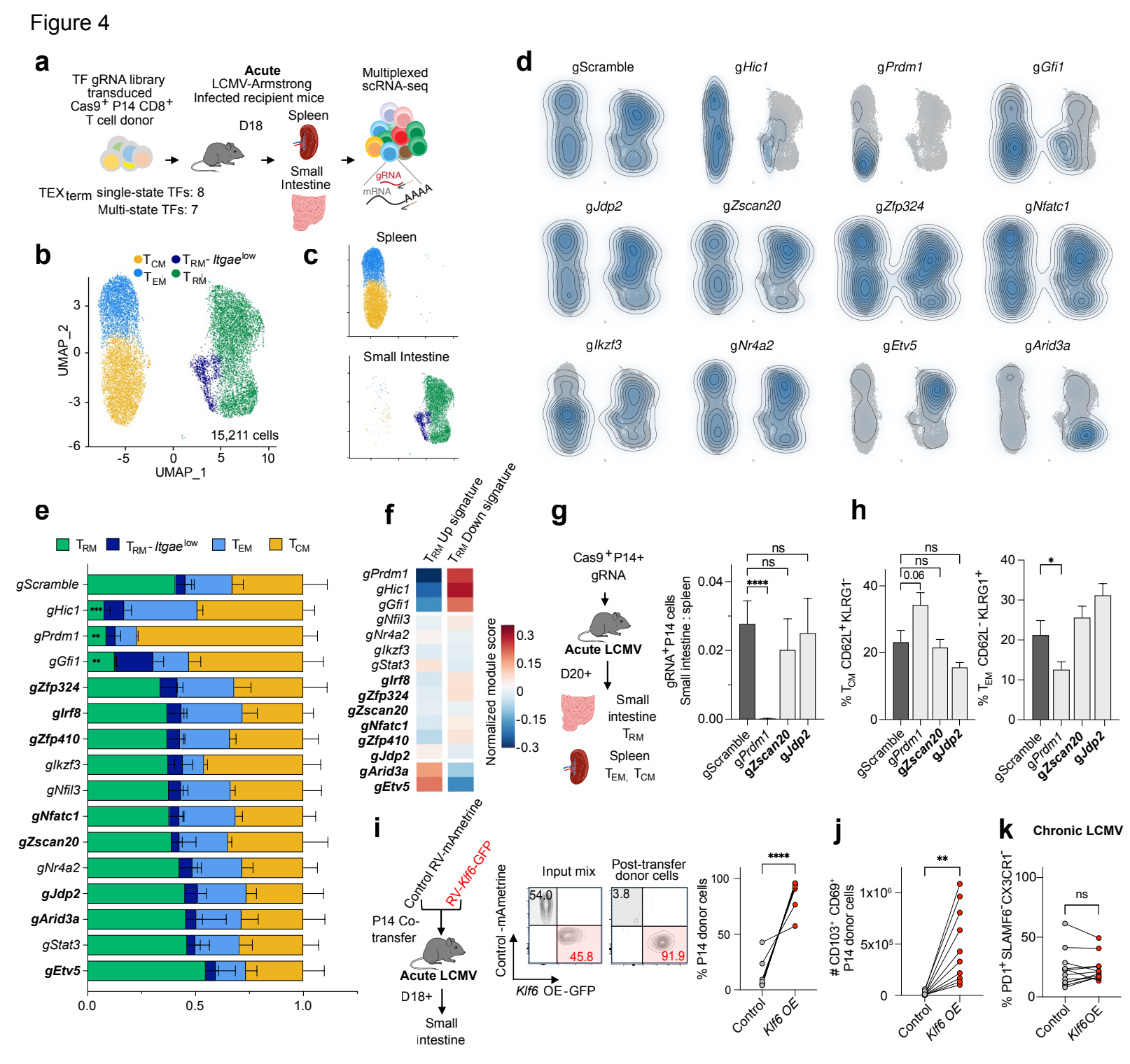
a
TF gRNA library transduced Cas9+ P14 CD8+ T cell donor
Acute LCMV-Armstrong Infected recipient mice
D18
Spleen
Small Intestine
Multiplexed scRNA-seq
gRNA
mRNA
AAAA
TEXterm single-state TFs: 8
Multi-state TFs: 7
b
TCM
TEM
TRM- Itgaelow
TRM
UMAP_2
UMAP_1
15,211 cells
c
Spleen
Small Intestine
d
gScramble
gHic1
gPrdm1
gGfi1
gJdp2
gZscan20
gZfp324
gNfatc1
gIkzf3
gNr4a2
gEtv5
gArid3a
e
TRM
TRM- Itgaelow
TEM
TCM
gScramble
gHic1
gPrdm1
gGfi1
gZfp324
gIrf8
gZfp410
gIkzf3
gNfil3
gNfatc1
gZscan20
gNr4a2
gJdp2
gArid3a
gStat3
gEtv5
f
TRM Up signature
TRM Down signature
gPrdm1
gHic1
gGfi1
gNfil3
gNr4a2
gIkzf3
gStat3
gIrf8
gZfp324
gZscan20
gNfatc1
gZfp410
gJdp2
gArid3a
gEtv5
Normalized module score
g
Cas9+ P14+ gRNA
Acute LCMV
D20+
Small intestine TRM
Spleen TEM, TCM
gRNA+ P14 cells Small intestine : spleen
h
% TCM CD62L+ KLRG1-
% TEM CD62L- KLRG1+
i
Control RV-mAmetrine
RV-Klf6-GFP
P14 Co-transfer
Acute LCMV
D18+
Small intestine
Input mix
Post-transfer donor cells
Control -mAmetrine
Klf6 OE-GFP
% P14 donor cells
j
CD103+ CD69+ P14 donor cells
k
Chronic LCMV
% PD1+ SLAMF6- CX3CR1-
Control
Klf6 OE

Figure 5

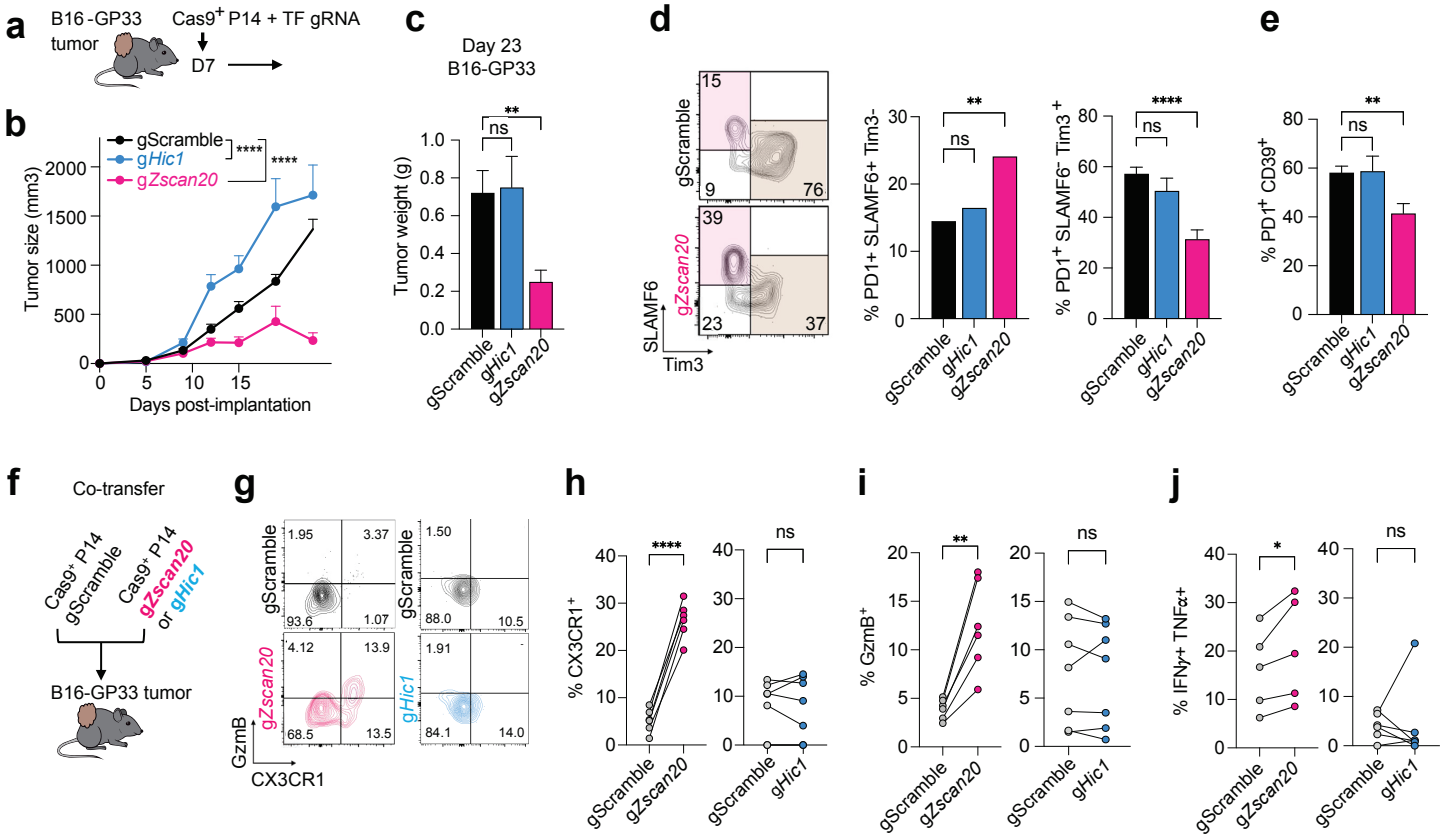
a
B16-GP33 tumor
Cas9+ P14 + TF gRNA
D7
b
gScramble
gHic1
gZscan20
Tumor size (mm3)
Days post-implantation
c
Day 23
B16-GP33
Tumor weight (g)
ns
**
d
gScramble
gZscan20
SLAMF6
Tim3
% PD1+ SLAMF6+ Tim3-
% PD1+ SLAMF6- Tim3+
e
% PD1+ CD39+
f
Co-transfer
Cas9+ P14 gScramble
Cas9+ P14 gZscan20 or gHic1
B16-GP33 tumor
g
GzmB
CX3CR1
h
% CX3CR1+
i
% GzmB+
j
% IFNγ+ TNFα+

Figure 6

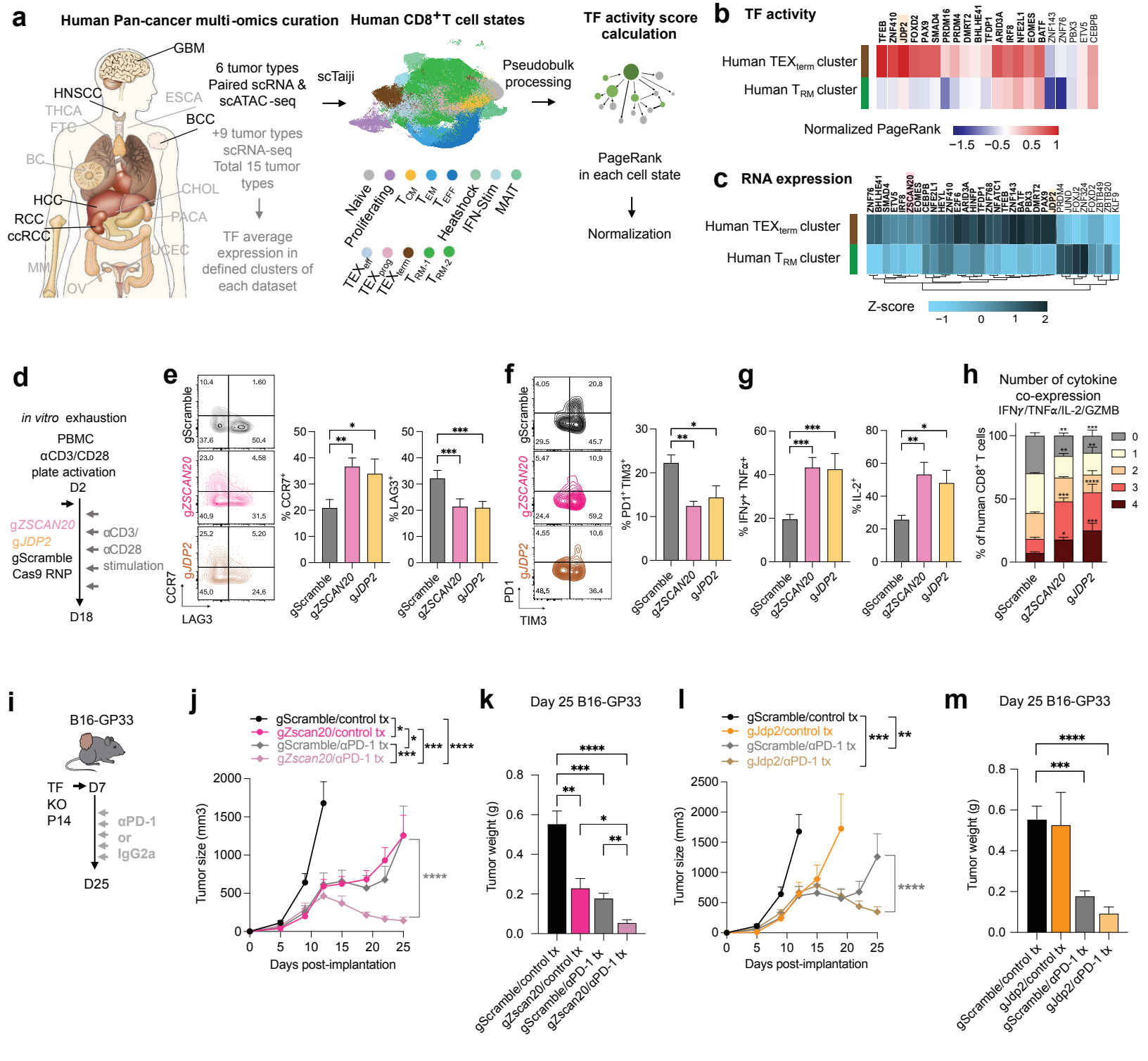
a
Human Pan-cancer multi-omics curation
Human CD8+T cell states
TF activity score calculation
GBM
HNSCC
THCA
FTC
ESCA
BCC
BC
CHOL
HCC
RCC
ccRCC
PACA
UCEC
MM
OV
6 tumor types
Paired scRNA &
scATAC-seq
+9 tumor types
scRNA-seq
Total 15 tumor
types
TF average
expression in
defined clusters of
each dataset
scTaiji
Pseudobulk
processing
PageRank
in each cell state
Normalization
Naive
Proliferating
TCM
TEM
TEFF
Heatshock
IFN-Stim
MAIT
TEXeff
TEXprog
TEXterm
TRM-1
TRM-2
b
TF activity
Human TEXterm cluster
Human TRM cluster
Normalized PageRank
−1.5 −0.5 0.5 1
c
RNA expression
Z-score
−1 0 1 2
d
in vitro exhaustion
PBMC
αCD3/CD28
plate activation
D2
gZSCAN20
gJDP2
gScramble
Cas9 RNP
αCD3/
αCD28
stimulation
D18
e
gScramble
gZSCAN20
gJDP2
CCR7
LAG3
% CCR7+
% LAG3+
f
PD1
TIM3
% PD1+ TIM3+
g
% IFNγ+ TNFα+
% IL-2+
h
Number of cytokine
co-expression
IFNγ/TNFα/IL-2/GZMB
% of human CD8+ T cells
i
B16-GP33
TF
KO
P14
D7
αPD-1
or
IgG2a
D25
j
gScramble/control tx
gZscan20/control tx
gScramble/αPD-1 tx
gZscan20/αPD-1 tx
Tumor size (mm3)
Days post-implantation
k
Day 25 B16-GP33
Tumor weight (g)
gScramble/control tx
gZscan20/control tx
gScramble/αPD-1 tx
gZscan20/αPD-1 tx
l
gScramble/control tx
gJdp2/control tx
gScramble/αPD-1 tx
gJdp2/αPD-1 tx
Tumor size (mm3)
Days post-implantation
m
Day 25 B16-GP33
Tumor weight (g)
gScramble/control tx
gJdp2/control tx
gScramble/αPD-1 tx
gJdp2/αPD-1 tx